2010

Transport Simulations of Carbon Monoxide and Aerosols from Boreal Wildfires during Arctas Using WRF-Chem

Walter Raymond Sessions

THE FLORIDA STATE UNIVERSITY

COLLEGE OF ARTS AND SCIENCES

TRANSPORT SIMULATIONS OF CARBON MONOXIDE AND AEROSOLS FROM BOREAL WILDFIRES DURING ARCTAS USING WRF-CHEM

By

WALTER RAYMOND SESSIONS

A Thesis submitted to the
Department of Meteorology
in partial fulfillment of the
requirements for the degree of
Master of Science

Degree Awarded:
Summer Semester, 2010

The members of the committee approve the thesis of Walter Sessions defended on April 15, 2010.

_____
Henry Fuelberg
Professor Directing Thesis

_____
Guosheng Liu
Committee Member

_____
Robert Hart
Committee Member

The Graduate School has verified and approved the above-named committee members.

ACKNOWLEDGEMENTS

The completion of this thesis required the work and attention of far more and greater minds than my own. The majority of my thanks go to my major professor, Dr. Henry Fuelberg. He had faith in my abilities at times when others did not, providing a career broadening array of opportunities in research. His respect for the fundamentals of science and strong work ethic drove my success within the graduate program here at Florida State University. Additionally, I would like to the other members of my committee, Drs. Guosheng Liu and Robert Hart. Dr. Phillip Cunningham, from the Los Alamos National Laboratory, and Mike Fromm, from the Naval Research Laboratory, provided a wealth of experience in simulating wildfires that directed the early stages of this study. A special thanks goes to members of the Jet Propulsion Laboratory, Dr. Ralph Kahn in particular, for providing amazing data analysis tools and plume data. Steven Peckham and the rest of the WRF-Chem support team should also be commended to their promptness and patience.

The members of the Fuelberg Lab also deserve thanks for maintaining my sanity during the long hours in the Love Building. The members packed into room 311, Donal Harrigan and Michael Porter, receive special notice for suffering my constant allergy related caterwauling and mood swings when acting as technical support. It will remain forever unknown if all of the lab's University of Florida football fans were intentionally put in the same, small room. I will also always cherish my friendships with Luke Peffers and Pete Saunders, long after I no longer have the ability to delete their data.

Finally, I would like to thank my family, who unblinkingly support all of my decisions. My parents, Drs. E. Hampton Sessions and B. Jean Young, for fostering my computer hobbies which now help me support myself. My sister Jocelyn, for giving me three beautiful nephews and always finding time to call. My brother, Dr. Hamp Sessions, Jr., for putting me ahead of the curve by always forcing me down the hard path, and his wife, Dr. Laura Sessions, for taking him off our hands. My oldest sister, Jennifer, for my entire Boston experience and truly believing that I had a beard in middle school. And lastly, my younger brothers, James and Hunter, for putting up with so many scientists.

This research was sponsored by the NASA Tropospheric Chemistry Program under Grant NNX0AH72G.

TABLE OF CONTENTS

LIST OF FIGURES

LIST OF TABLES

ABSTRACT

The Weather Research and Forecasting Model (WRF) was developed by the National Center for Atmospheric Research as the next generation mesoscale meteorology model. The inclusion of a chemistry module (WRF-Chem) allows transport simulations of chemical and aerosol species such as those observed during NASA's Arctic Research of the Composition of the Troposphere from Aircraft and Satellites (ARCTAS) during 2008. The ARCTAS summer deployment phase during June and July coincided with large boreal wildfires in Saskatchewan and Eastern Russia.

One of the most important aspects of simulating wildfire plume transport is the height at which emissions are injected. WRF-Chem contains an integrated one-dimensional plume rise model to determine the appropriate injection layer. The plume rise model accounts for thermal buoyancy associated with fires and the local meteorological stability. This study compares results from the plume model against those of more traditional injection methods such as filling the planetary boundary layer or a layer 3-5 km above ground level (AGL). Fire locations are satellite-derived from the GOES Wildfire Automated Biomass Burning Algorithm (WF_ABBA) and the MODIS thermal hotspot detection. Two preprocessing methods for these fires are compared: the prep_chem_sources method included with WRF-Chem, and the Naval Research Laboratory's Fire Locating and Monitoring of Burning Emissions (FLAMBE).

Satellite products from the AIRS, MISR and CALIOP sensors provide data for verifying the simulations. Observed near-source plume heights from MISR's stereo-height product are compared with the plume rise model's simulated injection heights. Long range plume transport is evaluated qualitatively in the horizontal using AIRS's total column carbon monoxide product. Qualitative vertical evaluation uses CALIOP's high vertical resolution and aerosol identification algorithm. Horizontal plume structures are further tested quantitatively using an object-based methodology.

The plume rise model produces the best agreement with satellite-observed injection heights. Filling the planetary boundary layer or the 3-5 km AGL layer with emissions exhibit less agreement with the observational plume heights. Results indicate that WRF-Chem can accurately transport chemical plumes throughout the ten-day simulation. However, differences in injection heights produce different transport pathways. Small differences in injection height are ameliorated when synoptic scale features such as warm conveyor belts quickly loft the emissions to higher altitudes. In scenarios where large scale lofting is delayed, the plume rise simulations creates the most accurate simulated plumes.

CHAPTER ONE
INTRODUCTION

The Arctic acts as a barometer for the atmosphere with many changes affecting the poles before the more populated middle and low latitudes (Arctic Climate Impact Assessment, 2004). The Arctic's lack of large population centers fosters the falsehood that it is a pristine environment. Unfortunately, the Arctic has experienced documented large scale pollution events since the 18th century (Garrett, 2006) with pilots reporting visibility reducing haze in the 1950's (Mitchell, 1957). Understanding the mechanisms behind pollution transport into the Arctic and its chemical composition is pivotal to assessing the threat of climate change.

Arctic pollution occurs seasonally, with the greatest episodic increases in particle concentration observed during the winter and spring months (Quinn et al., 2007; Shaw, 1995; Barrie, 1986). These events are caused in part by the strong winter thermal inversion in the lower troposphere that traps pollutants within the isentropic polar dome. Dry conditions that limit wet deposition also extend aerosol lifetimes. This concentration leads to the photochemical "Arctic Haze" observed after polar sunrise that can persist until May. Sulfate and organics are the major constituents of haze events, with NOx, volatile organic compounds, nitrates, black carbon (BC), dust aerosols and ammonium also present (Quinn et al., 2007; Solberg et al., 1996).

These species that are mostly transported from outside the region pose an array of environmental threats to the Arctic's radiation budget. Most familiar are the effects of greenhouse gases such as carbon dioxide that trap thermal radiation in the lower troposphere. Black carbon deposits on snow and ice sheets decrease the surface albedo, thereby promoting earlier melts and creating a positive warming feedback mechanism (Hansen and Nazarenko, 2004; Koch and Hansen, 2005; McConnell et al., 2007). More direct atmospheric warming is due to aerosols that absorb in the visible and thermal spectrum (Sharma et al., 2006; Quinn et al., 2008). Climate models have depicted surface temperature increases as great as 0.5˚C that have been attributed to enhanced arctic tropospheric ozone (Shindell et al., 2006).

Dynamic chemical transport models play a critical research and operational role in understanding source-receptor relationships between pollutants and the Arctic. Transport models can be functionally subdivided into "online" and "offline" categories depending on their integration with a host meteorological model. Offline models ingest winds for transport, and they sometimes include fields such as boundary layer height and turbulent kinetic energy to describe meso- and micro-scale processes. Offline models are run *ex post facto* and therefore cannot simulate aerosol or chemical energetic effects, such as radiative absorption by aerosols or latent heat release from chemical bonding, back into the meteorological fields. The FLEXPART Lagrangian particle dispersion model (Stohl et al., 1998, 2005) is an example of an offline

model that typically uses global winds from the European Centre for Medium-Range Weather Forecasts (ECMWF) or the National Oceanographic and Atmospheric Administration's Global Forecast System (GFS).

While requiring longer computational integration times, online models attempt to provide more accurate representations of atmospheric chemical and aerosol interactions. The Weather Research and Forecasting Model with Chemistry (WRF-Chem) (Grell et al., 2005) incorporates radiative and chemical feedbacks into the atmospheric energy budget that an offline model cannot do. WRF-Chem is a customizable, non-hydrostatic, mesoscale model that incorporates a subset of the modular parameterizations of dynamical, physical and chemical atmospheric behavior found in WRF. WRF-Chem utilizes mass and scalar fields on the same Eulerian grid, preventing unnecessary interpolation. A detailed description of WRF-Chem can be found in Grell et al. (2005), with study specific details found in Chapter 2 below.

Model-derived data have been used extensively to characterize pollution pathways. Stohl et al. (2006) used FLEXPART to develop a transport climatology that revealed three primary mechanisms for transport to the Arctic's lower troposphere: ascent outside the Arctic followed by settling (primarily from North America, Asia and Europe), low level transport with ascent within the Arctic (primarily from Europe), and continuous low level transport (primarily from Europe during winter). Klonecki et al. (2003) showed that transport into the Arctic is consistent with isentropic flow. Their modeled plume characteristics showed ascent along isentropic surfaces as the plume moved north. Adiabatic transport requires that low level arctic pollution must originate north of the arctic front, limiting potential external sources. Otherwise, low level pollutants must undergo strong diabatic cooling.

Boreal wildfires recently have been recognized as an important seasonal source of pollutants into the Arctic (Hegg et al., 2009; Kasischke et al., 2005; Andreae and Merlet, 2001; Crutzen and Andreae, 1990). Long range plume transport has been shown to have hemispheric influence and be a highly variable source of emissions (Wotowa et al., 2006; Damoah et al., 2004; van der Werf et al., 2003). While the total forest area burned within the tropics exceeds that of boreal fires, the trend during the past few decades has been a steady increase in boreal fires (Lavoue et al., 2000). Despite currently containing less burn area than tropical forest fires, boreal forests have denser growth and rich surface layers that increase the available organic fuel and emissions (Kasischke et al., 2005; Kasischke and Bruhwiler, 2002). Furthermore, Andreae et al. (2004) suggested that while removal processes are more efficient during the summer months, large aerosol loading from fires suppresses wet deposition, permitting significant aerosol transport.

The convective motions that often occur with wildfires increase the likelihood of emissions being lofted to the faster winds of the free atmosphere. While small surface emission sources with minimal excess energy often are turbulently mixed into the PBL (Labonne et al., 2007), plumes from crown fires have been

observed to maintain more cohesive structures into the free troposphere (Lavoue et al., 2000; Cofer et al., 1996; Generoso et al., 2007). This process relies on sensible heat flux from combustion and latent heat of condensation to enhance a plume's buoyancy (Freitas et al., 2007). Bryam (1959) estimated fire intensity as $I = cmr$, where c is the fuel's heat of combustion, m is the fuel mass, and r is the rate of spread. Previous research has suggested a linear correlation between I and emission injection height (Lavoue et al., 2000). Plumes often escape the boundary layer (Martin et al., 2009; Kahn et al., 2008) and can even reach the lower stratosphere during exceptionally explosive fire events, such as in cases of pyroconvection (e.g., Fromm, 2008; Trentmann et al., 2006). With intensity varying greatly between fires and wind velocity changing rapidly with height, releasing simulated emissions at realistic levels has been a crucial and difficult problem to successfully modeling plume transport (e.g., Colarco et al., 2004, Westphal and Toon, 1991).

Near source vertical plume distributions (the "injection height") often have been represented in transport models using empirical or arbitrary procedures. These methods have included linearly filling estimated injection columns (e.g., Damoah et al., 2004; Forster et al., 2001, Spichtinger et al. 2001), restricting emissions to the surface layers (Leung et al., 2007 ; Lamarque et al., 2003), assumed turbulent mixing by filling the planetary boundary layer (Fisher et al., 2010; Leung et al., 2007; Hyer et al., 2007), release in the upper atmosphere as occurs in pyroconvection (Hyer et al., 2007), or more complex distributions with emissions unevenly released at varying heights (Leung et al., 2007). Column filling methods attempt to mimic the turbulent and thermally induced mixing not explicit in the model by assuming, for example, that well mixed fire emissions will fill the PBL. Explicit resolution of three-dimensional microscale plume properties in an operational setting still is limited by current computational capabilities. To avoid such constraints, Freitas et al. (2007) embedded a one-dimensional plume-rise model into a larger scale grid to parameterize injection heights. Based on Lantham (1994), this 1D system uses meteorological model-derived column data to calculate atmospheric stability. Once vertical motion decreases to less than 1 ms^{-1}, a near equilibrium state is assumed, and the injection height is defined.

The Freitas et al. (2007) 1-d plume-rise model has been incorporated into WRF-Chem. This advance is important since many transport models rely on the coarse horizontal scale (e.g., 45-200 km) of global meteorological models for their transport parameters (e.g., Stohl et al., 2007; Damoah et al., 2004). While these models generally have produced satisfactory results, global models do compound interpolation error both spatially and temporally and can produce non-physical results within transport models (Stohl et al., 1995, 2004). The importance of WRF's increased resolution to improve the forecast skill of low level winds has been demonstrated by Mass et al. (2002).

The past decade has seen an increased number of satellite remote sensors whose data can be used in wildfire research. Many of these sensors are part of the A-Train constellation of polar orbiting platforms.

The MOderate-Resolution Imaging Spectrometer (MODIS) sensors aboard the Terra and Aqua satellites provide global scale active fire detection derived from the sensor's infrared bands (Justice et al., 2002, Giglio et al., 2003). Terra also houses the Multi-angle Imaging SpectroRadiometer (MISR) that can provide plume heights utilizing a stereo-height retrieval algorithm (Kahn et al., 2007). The lidar on the Cloud-Aerosol Lidar and Infrared Satellite Observation (CALIPSO) satellite provides high vertical resolution aerosol and cloud identification within a footprint that is 100 m across track (Winker et al., 2004). Labonne et al. (2007) utilized CALIPSO's Cloud-Aerosol Lidar with Orthogonal Polarization (CALIOP) retrievals to represent the total emission plume by assuming that the chemical and aerosol constituents were collocated. Although the Atmospheric InfraRed Sounder (AIRS) on Aqua provides poor vertical resolution, its data have been used to investigate the horizontal extent of combustion products such as carbon monoxide (e.g., Peffers et al., 2009; Zhang et al., 2008; Stohl et al., 2007).

The present study evaluates the ability of WRF-Chem's plume rise model to diagnose the injection heights of fire byproducts during NASA's Arctic Research of the Composition of the Troposphere from Aircraft and Satellites (ARCTAS) campaign in 2008 (Jacob et al., 2010). Two preprocessing methods for preparing biomass burning emissions are investigated; the standard WRF-Chem package (Prep_chem_sources) and the Naval Research Laboratory's (NRL) Fire Locating and Monitoring of Burning Emissions (FLAMBE). We compare injection heights from the plume rise model with those where pollutants are strictly injected within the boundary layer or between 3-5 km above ground level (AGL). We also evaluate the ability of WRF-Chem to model the downwind evolution of fire plumes. Model-derived plume characteristics are compared with those observed by satellite data. MISR- and CALIOP-derived products are used to define the vertical characteristics of plumes, with AIRS evaluating their horizontal extent.

Chapter 2 provides details about the WRF-Chem model and satellite products. It also contains details and assumptions about the methodology and evaluation tools. Results are found in Chapter 3, while Chapter 4 contains the summary and conclusions.

CHAPTER TWO

DATA AND METHODOLOGY

2.1 DOMAIN

Our research domain was selected based on observational and modeling considerations. The domain was centered on the geographic North Pole, extending over most of the Northern Hemisphere, and using a polar stereographic projection (Fig. 1a). Since our goal was to explore the transport of emissions into the Arctic, major historic source regions of biomass burning and anthropogenic emissions were located in the domain, including Russia, Alaska, Canada, and eastern Europe. These locations were placed far enough within the domain to minimize lateral boundary error in accordance with Warner et al. (1997).

The ARCTAS summer phase during June and July 2008 coincided with the outbreak of boreal wildfires in Saskatchewan and eastern Russia. In particular, a Siberian outbreak from 28-30 June (Fig. 1b) produced emissions that were observed to pool over Asia prior to being transported over the Pacific Ocean and into the Arctic. Summer flow patterns largely were within climatological norms except that a quasi-stationary polar low was displaced toward northern Russia, thereby enhancing transport pathways into the Arctic (Fuelberg et al., 2010). While not as intense as those in Russia, the Canadian fires over Saskatchewan and the northern territories produced outflow to Greenland and Europe during the same period. Our ten day model integration encompassed this period of active fires from 28 June – 8 July 2008.

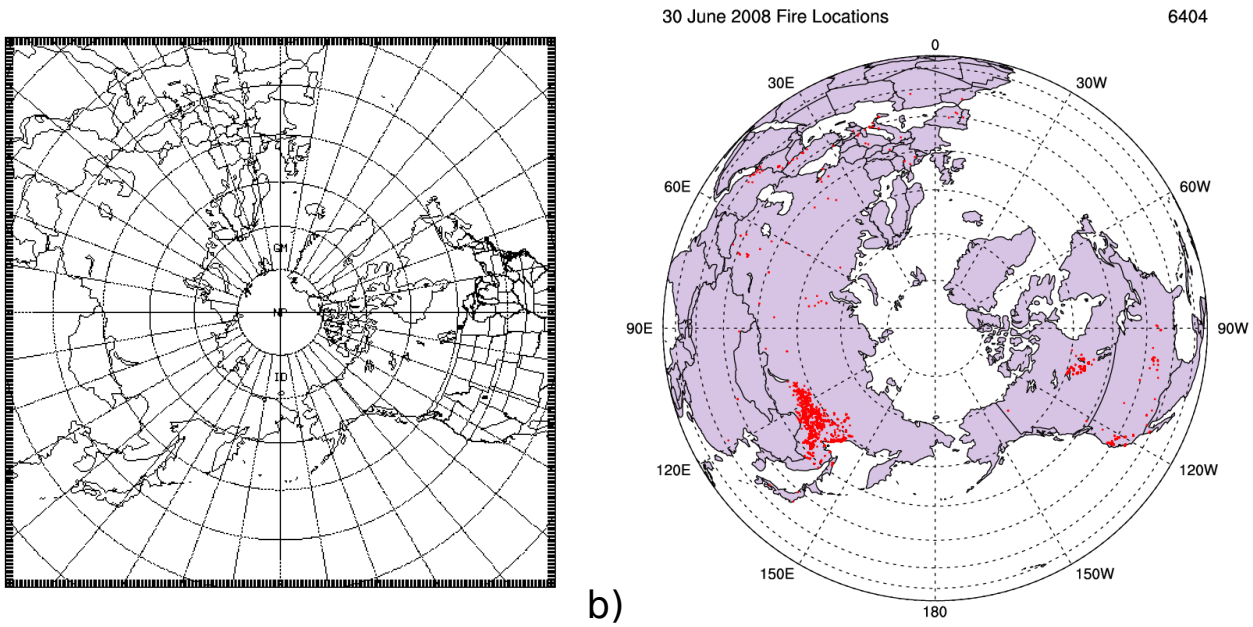

Fig 1. a) WRF-Chem domain and b) satellite-derived fire locations on 30 June 2008 during major Siberian and Canadian outbreaks.

2.2 WRF-CHEM

2.2.1 Initial and Boundary Conditions

Our transport simulations were performed using WRF-Chem version 3.1.1 which is based on the Advanced Research WRF (ARW) core developed by the National Center for Atmospheric Research (NCAR) (Shamarock et al., 2008). WRF is a non-hydrostatic, mesoscale model utilizing 2nd and 3rd order Runge-Kutta time integration schemes. WRF-Chem supports several physical, dynamic, and chemical parameterizations; however, not all of the packages available within the standard WRF (i.e., without chemistry) have been integrated into WRF-Chem (Grell et al., 2005). To simulate turbulent chemical transport within the boundary layer, our configuration used the Yonsei University PBL parameterization which diagnoses PBL height from the buoyancy profile (Hong et al., 2006). We used a horizontal grid resolution of 45 km with 50 vertical sigma levels packed near the surface and mean jet stream levels. Further information about model configuration is found in Table 2.

Meteorological boundary and initial conditions for our WRF-Chem simulations were interpolated from the National Centers for Environmental Prediction (NCEP) Global Forecast System (GFS; Global Climate and Weather Modeling Branch, 2003). GFS is a spectral model operating on an approximate 0.5 × 0.5 deg Gaussian grid with 64 vertical sigma levels.

Table 1. WRF-Chem domain and parameterization settings used in this study.

Field	**Setting**
Horizontal Resolution	45 km
Vertical Levels	50 non-linear sigma levels
Shortwave Radiation	Goddard
Longwave Radiation	RRTM
Surface Layer Physics	MM5 Similarity
Land Surface Physics	Noah
Planetary Boundary Layer	YSU
Cumulus Parameterization	Grell-Devenyi

2.2.2 Source Emissions and Chemistry

The gas phase chemistry mechanisms in WRF-Chem originally were developed for the Regional Acid Deposition Model, version 2 (RADM2, Chang et al., 1991). Although the model can simulate dozens of organic and inorganic species, we focused on carbon monoxide as a gas phase tracer of the biomass burning plumes. Initial and boundary conditions were represented by an idealized, northern hemispheric, mid-latitude, clean environmental profile from the NOAA Aeronomy Lab Regional Oxidant Model (NALROM, Liu et al., 1996). The parameterization of aerosols was incorporated from the Modal Aerosol Dynamics Model for Europe (MADE, Ackermann et al., 1998) with the Secondary Organic Aerosol Model (SORGAM) simulating the formation of secondary organic aerosols (Schell et al., 2001).

Global emissions recently have been incorporated into WRF-Chem. Anthropogenic emissions are based on the 0.5 × 0.5 deg REanalysis of the TROpospheric (RETRO) chemical composition over the past 40 years dataset (Schultz, 2008; http://retro.enes.org/index.shtml). The historical RETRO inventories merge aircraft, surface, and satellite measurements into a single dataset at a monthly temporal resolution. WRF-Chem includes a package to integrate these inventories onto the desired model grid.

Biomass burning emissions were similarly mapped but based on GOES and MODIS satellite retrievals. The GOES Wildfire Automated Biomass Burning Algorithm (WF_ABBA) relies on the method of Matson and Dozier (1981) to identify sub-pixel anomalies in the thermal infrared band that are associated with fires. Provided by the University of Wisconsin-Madison Cooperative Institute for Meteorological Satellite Studies (CIMSS), WF_ABBA provides half-hourly hot-spot identification for the majority of the Western Hemisphere. For global data, MODIS sensors aboard the Aqua and Terra satellites identify fires utilizing a method similar to WF_ABBA. Enhanced filtering limits false positives and increases the detection of cooler fire pixels (Giglio et al., 2003). MODIS products were produced by a joint NASA/University of Maryland-College Park (UM-CP) project and were available through the NASA Goddard Rapid Response System (http://rapidfire.sci.gsfc.nasa.gov/). Aqua and Terra fly in near-polar orbits with ascending and descending equator crossings at 1:30 and 10:30 LST, respectively. These orbits limit the temporal resolution of their active fire products.

Satellite-derived fire products were prepared using two preprocessing methods. WRF-Chem's officially supported package, prep_chem_sources (PCS), was developed and made available by the Brazilian Centro de Previsao de Tempo e Estudos Climaticos (CPTEC). This module primarily relies on user supplied geographic coordinates for each wildfire, which for our study came from CIMSS and UM-CP. Emission factors from Andreae and Merlet (2001) account for variation in surface types. When the fire radiative power or burn area are not supplied, PCS assumes an area of 228,000 m^2 per fire grid point.

The second source of biomass burning emissions was based on the Fire Locating and Modeling of Biomass Burning Emissions (FLAMBE) dataset (Reid et al., 2009). A joint Navy, NASA, NOAA, and university project, FLAMBE provides carbon and aerosol emissions at hourly intervals. Similar to PCS, fire data are from the WF_ABBA and MODIS active fire products. Emissions are calculated by matching fire locations to a 1 km land use database. FLAMBE simulates diurnal variability by releasing 90 percent of the emissions between 0900 – 1900 LST. The reported burn area also is used to simulate this temporal variability, splitting an estimated 625,000 m^2 burn area per fire into 24 hourly segments that are proportional to diurnal fire activity (i.e., a larger burn area in the afternoon than overnight). This correction is necessary since a MODIS sensor may only cross a specific location four times per day. Hourly FLAMBE emissions were converted and regridded to be consistent with our WRF-Chem configuration.

2.2.3 Injection Height

The combustion of vegetation increases the surface heat flux and buoyancy of a rising plume. Entrainment of environmental air into the column results in rapid cooling, causing near-source plume temperatures to be only slightly warmer than the environment. Buoyancy also is affected by radiative cooling and latent heat release if the plume reaches the lifting condensation level (LCL). Strong horizontal winds can enhance the entrainment processes and prevent the plume from reaching the LCL (Freitas et al., 2009; Martin et al., 2009). Strong winds also produce enhanced turbulent mixing in the boundary layer. Regardless, the influence of the horizontal wind on vertical plume development is not considered in the WRF-Chem 3.1.1 plume rise model (S. Freitas, 2009 personal comm).

WRF-Chem's one-dimensional plume rise model is based on the continuity equations for water in all phases, the vertical equation of motion, and the first law of thermodynamics (Latham, 1994; Freitas et al., 2007). To reduce the limitations of 1-d simulation, the model includes parameterizations for autoconversion (Berry, 1968), ice formation (Ogura and Takahashi, 1971), cloud microphysics and accretion (Kessler, 1969) with entrainment defined as proportional to vertical velocity. To estimate heat flux, fires are divided into four surface categories based on the WRF land use dataset: savanna, grassland, tropical and extra-tropical forests. Simulated atmospheric sounding data for the plume rise model are computed every hour at each grid point containing an active fire. Updated emission layers are produced based on column stability.

To evaluate the efficacy of the WRF-Chem plume rise model, we used traditional emission schemes in separate model runs. Two column filling methods were used: emissions throughout the PBL and from 3 km to 5 km. These methods previously have been used to estimate turbulently mixed surface emissions and lofted emissions, respectively. Since injection levels vary by location and time of day, a WRF simulation

first was run to provide approximate PBL and lofted layer heights at the individual fire locations. Emissions then were linearly distributed within the input layers for the chemically enabled WRF-Chem runs.

2.3 VERIFICATION METHODS

To judge the accuracy of the simulated aerosol and carbon monoxide transport from the wildfires, we required observations of near-source injection heights as well as horizontal and vertical plume specifications after long range transport. Accepting the limitations in remotely sensed data, particularly at high latitudes, we used the following satellite products to represent the chemical state of the atmosphere.

2.3.1 MISR Data

To evaluate WRF-Chem's near-source injection heights, we used stereo-height products from the Multi-angle Imaging SpectoRadiometer (MISR) aboard the NASA Terra satellite. MISR observes four spectral bands using nine cameras (four forward, four aft, plus nadir) to view features at multiple incidence angles with minimum temporal lag. With several viewing angles, various parameters can be calculated including geometric aerosol properties such as single-scatter albedo, shape within features, and most importantly, feature altitudes.

MISR stereo-height products are derived in two steps (Muller et al., 2002, Diner et al., 1999, Kahn et al., 2006). The fore and aft near-nadir cameras are stereo-matched to compare the regions of maximum reflectance. These views are used to estimate feature height using the geometry of the scene. Once the layer altitude estimation is completed, corrections based on estimated winds then are applied. Wind speed estimates are based on the 70.5^{o}, 45.6^{o} and nadir cameras to an accuracy of $\pm$ 3 ms^{-1}. If the estimated winds from the fore and aft camera couplets do not exceed quality control limits when compared, they are applied to create the wind-corrected, stereo-height product on a 1.1 km grid.

Plumes were processed and digitized as part of the ongoing MISR Plume Height Climatology Project at the NASA Jet Propulsion Laboratory. Using the MISR INteractive eXplorer (MINX) software (Nelson et al., 2008), nearly 1600 plumes were analyzed over Siberia and Canada during 2008; 250 plumes were identified during our ten day model integration period (http://www-misr2.jpl.nasa.gov/EPA-Plumes/). MINX users manually identify individual plumes using the combination of MODIS fire pixels and the nine camera views provided by MISR. Once individual plume boundaries are defined, MINX calculates the stereo-height product of the enclosed feature, digitizing values such as maximum and median feature heights, pixel distance from source, and wind speed. To compare the MISR-derived plumes with those from the WRF-Chem plume rise model, the maximum plume heights were matched to the nearest model grid point in

space and time. If multiple plumes are located within the same WRF-Chem grid cell, the average of their contributing MISR heights is assigned.

2.3.2 AIRS Data

The Atmospheric Infrared Sounder (AIRS) on the Aqua satellite provides nearly 70 percent coverage of the Earth's surface on a daily basis (McMillan et al., 2005). With such a large coverage field, the AIRS total column carbon monoxide (CO) product allowed us to evaluate the downwind evolution of the simulated horizontal plumes. AIRS total column CO data are the weighted sum of the combined infrared and microwave CO layer retrievals up to 0.005 hPa. Previous aircraft based studies have shown non-polar retrieval uncertainty to be 15-20% at 500 hPa (McMillan et al., 2005). The CO products have not yet been validated over polar regions, suggesting uncertainty estimates closer to 10-50% at 500 hPa (http://disc.sci.gsfc.nasa.gov/AIRS/documentation/v5_docs/AIRS_V5_Release_User_Docs/V5_CalVal_Status_Summary.pdf). AIRS CO data at very high latitudes currently show a low bias (J. Warner, personal comm.). Validation over the Arctic was outside the scope of the current research.

The recommended filtering procedures were applied to the AIRS CO product to increase their quality (AIRS Version 5.0 Released Files Description). Total column CO data were restricted to the best retrievals (Qual_CO = 0), representing values obtained primarily from the retrievals instead of the *a priori* profiles and accounting for error introduced by atmospheric water vapor. The data then were simplified into normalized fields for comparison with WRF-Chem.

To quantify WRF-Chem's forecasting skill compared to AIRS, we used the Model Evaluation Tools (MET) package produced by the Developmental Testbed Center (DTC) (http://www.dtcenter.org/met/users/). MET contains tools for comparing gridded model output to regularly or irregularly spaced measurements or other gridded model output. The Method for Object-Based Diagnostic Evaluation (MODE) tool in MET is distinctive from traditional evaluation methods. Point-to-point comparisons between collocated grid points can lead to double penalties if forecasts are even marginally displaced; however, MODE uses fuzzy logic to compare “objects.” These objects are any cohesive field (e.g., CO, for our study). Skill is assessed by identifying and evaluating the similarity between matched objects in the observed and forecast fields. AIRS total column CO was mapped to the same model grid as the simulated WRF-Chem total column CO. MODE uses these inputs to compute statistical skill scores for the forecast.

2.3.3 CALIOP Data

The CALIOP sensor aboard CALIPSO provides higher resolution atmospheric profiles than most other satellite-derived products. CALIOP is an active lidar sensor that utilizes polarized, dual-channel (532 and 1064 nm) attenuated backscatter to directly observe cloud and aerosol features (Winker et al., 2004). CALIPSO is in a Sun-synchronous, polar orbit 705 km above the Earth's surface.

CALIOP's aerosol and cloud products were produced by NASA using a multi-step discrimination process. First, the locations of features are found using profiles of 532 nm attenuated backscatter ratio. An adaptive thresholding technique discerns clear air from the enhanced ratios of features. Once a feature is identified, clouds and aerosols are separated using the ratio of backscatter coefficients in the 1064 nm and 532 nm channels. Cloud particle sizes are large relative to the lidar's wavelength, producing little difference between the two channels and a ratio close to unity. Conversely, with the exception of dust, the much smaller aerosol particles produce an enhanced signal in the 532 nm channel and a ratio less than one. These features then are further typed by subclass: ice, liquid, and mixed phase clouds or dust, smoke, and polluted aerosol layers.

In evaluating WRF-Chem's long range vertical accuracy, we qualitatively used the vertical feature mask (VFM) and the 532 nm attenuated backscatter products (Vaughan et al., 2004). The VFM provides a simplified view of a retrieval swath. Horizontally and vertically averaged feature locations and types are color-coded to facilitate the basic analysis.

2.4 TEST CASES

Six WRF-Chem simulations were run to evaluate the various emission sources and injection height strategies. The two emission preprocessing methods, Prep_chem_sources (PC) and FLAMBE (FB), were run with three injection height schemes: plume rise (PLR), filling the boundary layer (PBL), and releasing between 3-5 km AGL (35K). Subsequent references will refer to these combinations by their abbreviations (i.e., PC_PLR, FB_35K, etc., Table 2).

Table 2. Configurations used during our study as defined by the biomass burning preprocessor and injection layer scheme.

	1D Plume Rise	Filled PBL	Filled 3-5 km Layer
Prep_chem_sources	PC_PLR	PC_PBL	PC_35K
FLAMBE	FB_PLR	FB_PBL	FB_35K

CHAPTER THREE

RESULTS

We now examine the simulated plumes produced by the WRF-Chem runs. The meteorological features that produce plume transport are described first. We then evaluate the injection heights calculated by the two WRF-Chem plume rise configurations (FB_PLR and PC_PLR) by comparing them with plume heights diagnosed by MISR. We next determine which biomass burning emission preprocessor produces results that agree best with the MISR observations. Finally, simulated long range plume transport is compared with plume features revealed by AIRS and CALIOP.

3.1 METEOROLOGY

The topography of the study region and the meteorology during the simulation period are important in understanding the results that follow. Most of the observed fires were located on the Stanovoy Mountain range (Fig. 1b) that extends westward from the Sea of Okhotsk (Fig. 2). Much of the mountain range lies between 700 to 1500 m above sea level (ASL). The local orography and the transit of a mid-latitude cyclone produced thunderstorms in the area during the days preceding our integration period. The associated lightning likely was responsible for the dramatic increase in fire activity.

The quasi-stationary polar low was anomalously displaced towards Siberia during ARCTAS (Fig. 3a,b; Fuelberg et al., 2010). The counter-clockwise winds around the low provided one of two primary transport pathways off the Asian continent. The northern path toward the Arctic begins over the Chukotski Peninsula, located on the opposite side of the Bering Straight from Alaska (Fig. 2). The southern path is created by an exiting mid-latitude cyclone southeast of the Kamchatka Peninsula. Once this mid-latitude cyclone moved offshore, high pressure ridging over the Stanovoy Range cleared the sky, dried the surface, and promoted fire activity. The stream bifurcation between these two paths begins at the saddle point between the two low pressure systems, most clearly visible in the 850 hPa streamline analysis on 29 June (arrow in Fig. 3a). However, the northern pathway does not fully form until the saddle point degrades on 6 July (Fig. 3c). A mid-latitude cyclone approaches the Aleutian archipelago on 2 July before merging with the Aleutian low on 6-8 July. The quasi-stationary low retains its position during most of the simulation period. It briefly is displaced southward by the mid-latitude cyclone during 1-2 July, but returns offshore by 6 July.

The fires in Canada and Alaska were ignited by a succession of cyclonic storms beginning with a shortwave trough on 28 June that passed over Saskatchewan (Fig. 3e-h). This cyclone was followed by a second system that also initiated thunderstorms, including a pyroconvective cell on 29 June in the Northwest

Territories (M. Fromm, personal comm.). The flow downwind of the Canadian fires was dominated by two semi-permanent lows located over Ontario/Quebec and southeast of Greenland, respectively. This combination produced a transport pathway toward the North Atlantic, limiting transport into the Arctic.

Accurately modeling the atmospheric state is important for reasons other than just transport. Atmospheric stability plays an important role in simulating injection heights within WRF-Chem's plume rise model. To demonstrate the role of atmospheric stability, Fig. 4 shows two simulated soundings over boreal plumes. Fig. 4a depicts a classical subsidence inversion that creates a stable layer near ~1.5 km AGL. The maximum height of the WRF-Chem simulated injection layer reaches 1137 m, in good agreement with the 1295 m height observed by MISR. Conversely, the injection layer is overestimated in the conditionally unstable WRF-Chem sounding in Fig. 4b. MISR observed an aerosol layer at 2501 m, well below the simulated 5353 m heights. Inaccuracies within the simulated meteorological stability profile therefore can be compounded by the plume rise mechanism to produce erroneous emission layers.

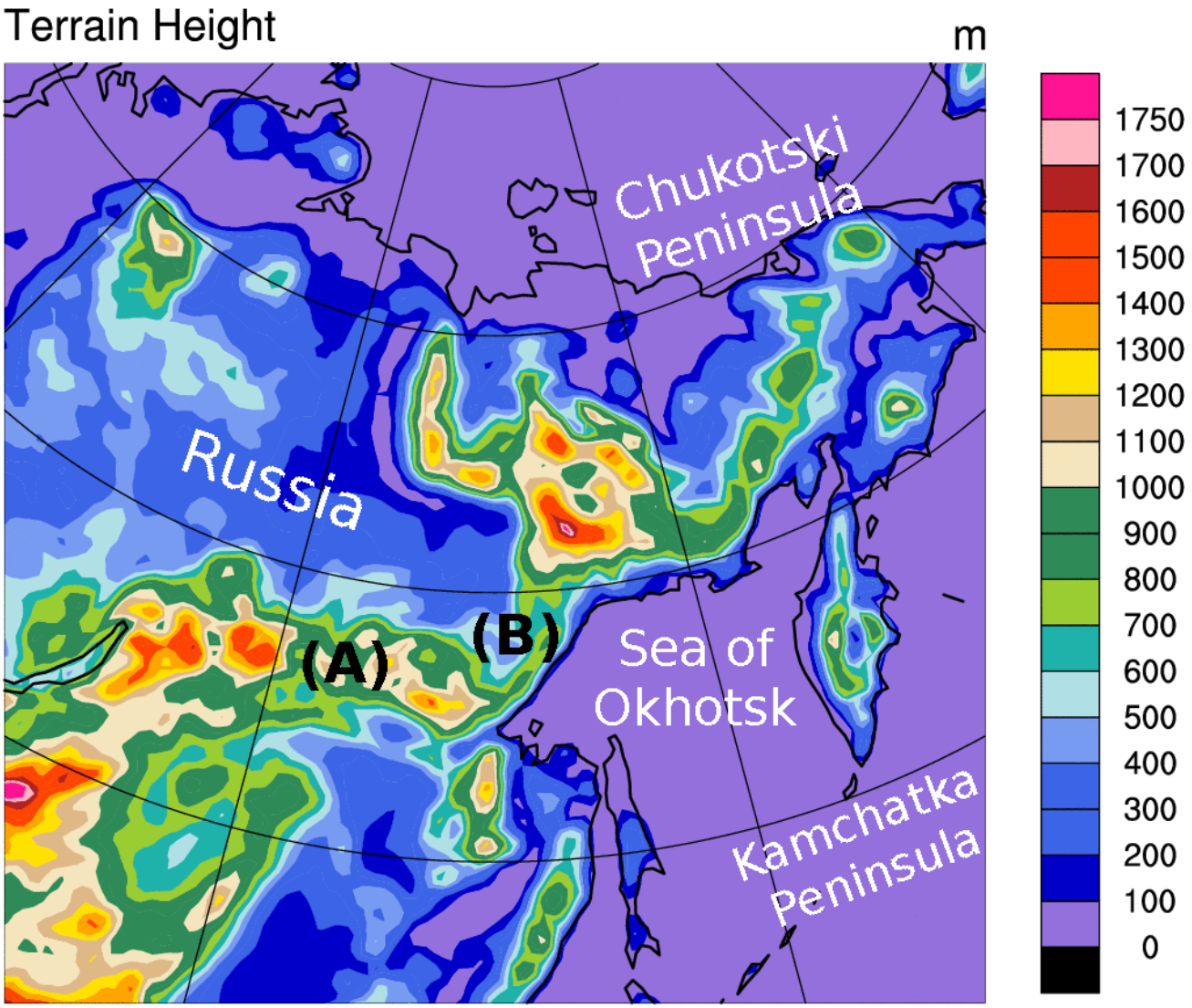

Fig. 2. Topographic map of northeastern Asia. Observed fires were primarily on the Stanavoy Mountains (labeled A) and the Dzhugdzhur coastal range (labeled B) west of the Sea of Okhotsk.

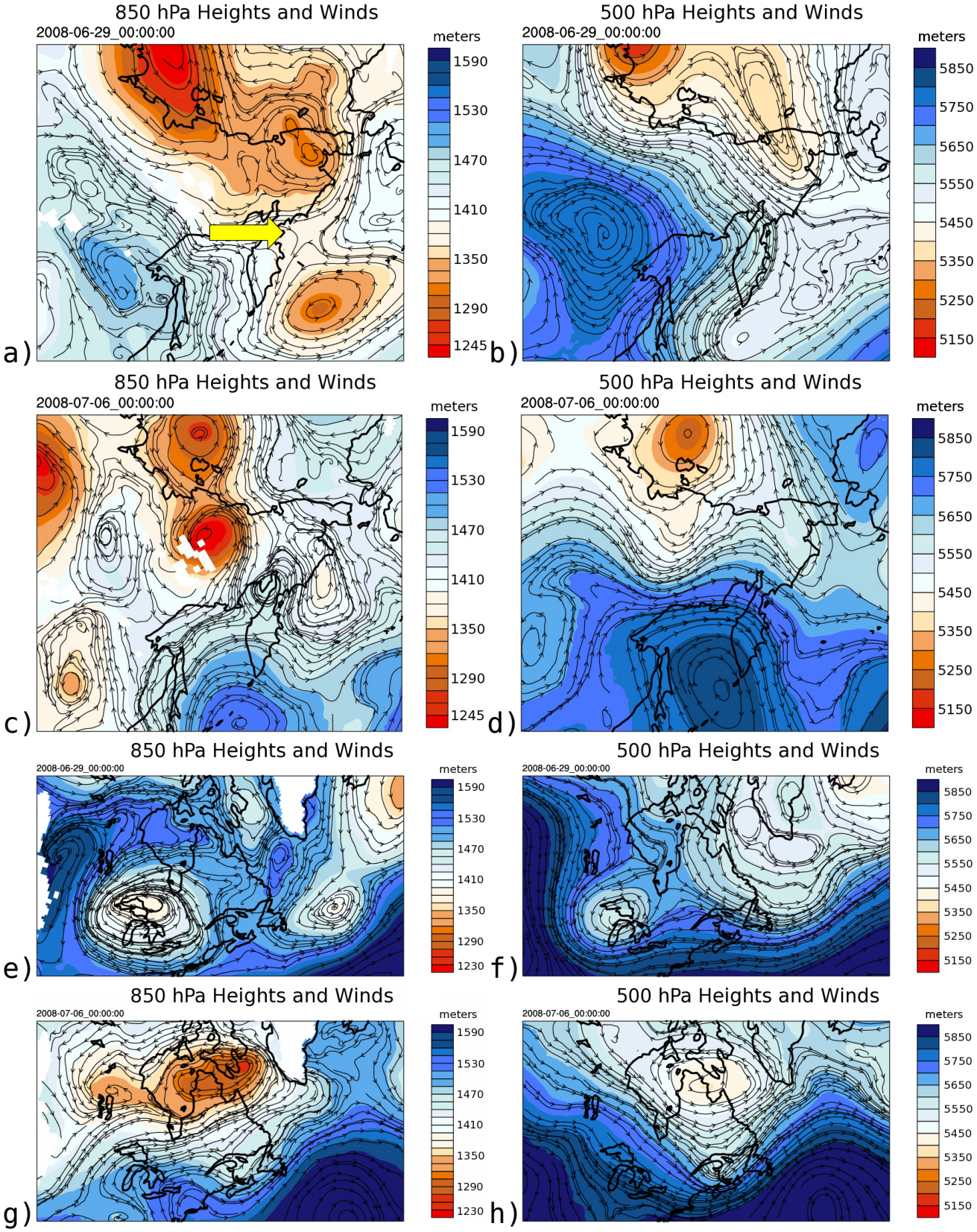

Fig. 3. Geopotential heights (color filled lines) and streamlines over northeastern Asia and the North Pacific Ocean (a-d) and North America (e-h) at 850 hPa (left column) and 500 hPa (right) for 0000 UTC 29 June and 0000 UTC 6 July 2008. The arrow in panel a) denotes the saddle point where the north and south pathways from Russia split. Note that streamlines and trajectories are not equivalent.

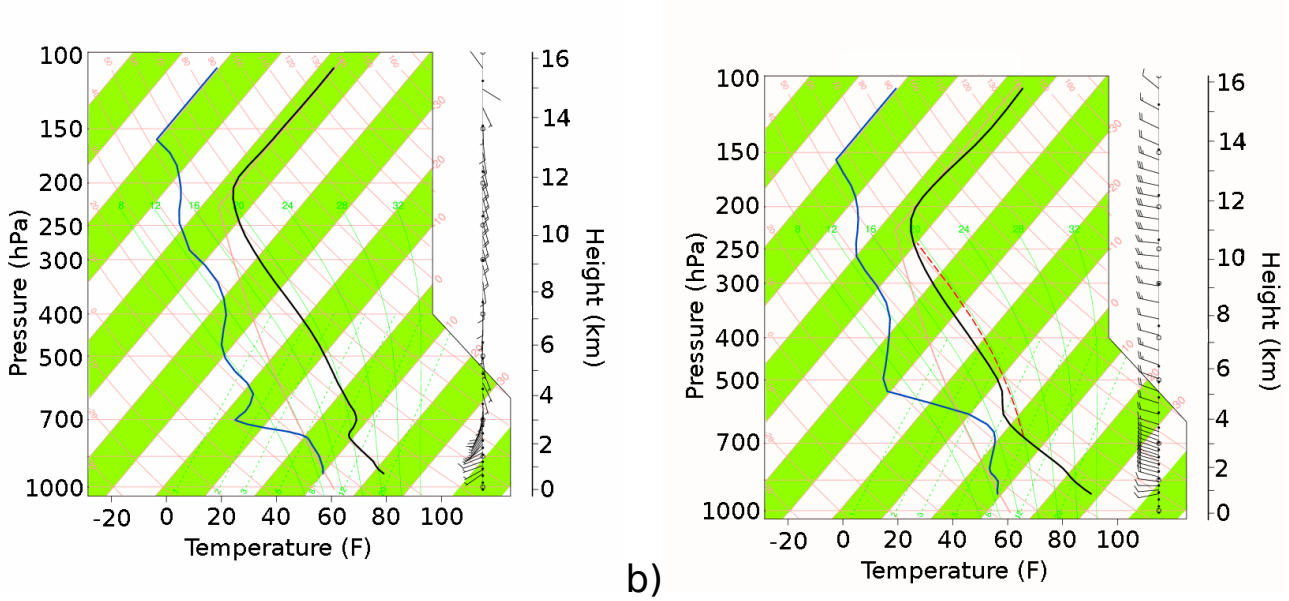

Fig. 4. Sample soundings from WRF-Chem (PC_PLR) at example locations of a) low (1137 m) and b) high (5353 m) injection heights. Temperature and dew point are in black and blue, respectively. Convective Available Potential Energy (CAPE) is indicated by a dashed red line.

3.2 INJECTION HEIGHT COMPARISONS

The MISR plume heights calculated by MINX allow us to evaluate the ability of WRF-Chem's two plume rise configurations (FB_PLR and PC_PLR) to produce appropriate injection layers. Fig. 5 is an example of a Canadian smoke cloud observed by MISR on 30 June 2008. A maximum and median height were derived for each plume (Fig. 5c), representing a plane fit to the wind-corrected heights after removing values outside 1.5 standard deviations. We used the maximum planar height for each fire in our comparisons with WRF-Chem. Other results (not shown) indicated that this maximum top produced better Spearman correlations (r_s = 0.45) with the WRF-Chem plumes than did median values (r_s = 0.11). In addition, choosing the MISR median height potentially would leave significant emissions above the assumed injection layer top (Fig. 5c), which would be inappropriate when comparing with discrete model levels.

Considering the entire ten day simulation, the FLAMBE emissions (FB_PLR) demonstrate better agreement with MISR's maximum stereo-heights than do heights from PC_PLR, e.g., a Spearman correlation (r_s) of 0.45 versus 0.07 (Fig. 6). FB_PLR also simulates 54 percent of the plumes within the estimated ± 560 m error range of MISR stereo-heights, compared to 41 percent from PC_PLR. Differences between the injection heights produced by PC_PLR and FB_PLR stem from parameterizing the entrainment of environmental air. The plume rise model parameterizes entrainment based on an inverse relationship with plume radius, i.e., the larger the plume radius, the less effect environmental air has on the fire's thermal anomaly. This effect can be seen in Fig. 6b where the constant area (22.8 ha) that is assumed by PC_PLR for MODIS fire detections limits the tops of the simulated plumes to between 1.3 km and 3.0 km.

Conversely, most tops from FB_PLR (Fig. 6a) range from a few hundred meters to 3 km, based on plume sizes ranging from 1.25 to 62.5 ha. Because of MISR's descending daytime overpass, Northern Hemisphere retrievals such as ours occur before 1030 LST. Since retrieval times are compared with the nearest model output time, the smaller morning burn areas in FB_PLR produce better agreement with the satellite retrievals. Based on this more realistic portrayal of injection heights, the long range transport simulations described in later sections will be limited to using the FLAMBE (FB) emission data.

The distribution of WRF-Chem injection heights during the ten day integration period, i.e., not just those matched to MISR retrievals, shows that FB_PLR produces somewhat lower injection layers than PC_PLR (Fig. 7a,b). Both produce most injection heights below 3 km in agreement with MISR (Fig. 7c). However, both median simulated injection heights are ~2.1 km, while MISR's median height is closer to 1.5 km. Thus, the median simulated injection heights are ~600 m higher than observed by MISR. This is partially caused by a sampling bias; the total number of observed MISR plumes is less than half the simulated plumes (Fig. 7c) because the MISR plume heights are derived only from the Terra satellite, while fire locations for WRF-Chem are obtained from Aqua, GOES, and Terra. The observed (simulated) Russian plumes, which average ~900 m (~1.5 km) lower than the Canadian plumes, comprise 96 percent (87 percent) of the MISR (WRF-Chem) plumes during our ten day period. This greater representation (96 percent in the observations versus 87 percent in the simulations) of the taller Canadian plumes in the model data produces a higher average injection height than observed by MISR.

As a simpler alternative to utilizing an embedded 1-d plume model as in WRF-Chem, numerous previous studies have released emissions between the surface and the planetary boundary layer (e.g., Fisher et al., 2010; Leung et al., 2007; Hyer et al., 2007). To examine simulated emission injection that is limited to the PBL, we first matched MISR heights to our model grid points using the same method described in Chapter 2 for comparisons with injection heights. Once the MISR heights were matched to grid points, we compared them with the WRF-Chem PBL height at each location. Results show that most of the satellite-derived emission layers are above the simulated PBL (Fig. 8a). Thus, there is a strong preference for injection into the free troposphere. This contrasts with the research of Kahn et al. (2008) who compared MISR stereo-heights to GEOS-4 simulated PBL heights. They found that although between 5 – 18% of MISR plumes extended above the PBL, the majority remained below. It should be noted that Kahn et al. utilized median plume heights, whereas we employed maximum heights. They also compared many more MISR plumes, more than 600, than the 250 during our ten day period. Labonne et al. (2007) found most emissions remaining in the PBL. They were above the PBL only in cases of large scale lofting. However, Kahn et al. (2008) noted that Labonne et al. (2007) used only CALIOP data, making the data highly dependent on how close the lidar profile was to the source. In our study, both the FB_PLR and PC_PLR

plume rise models simulate most of the maximum injection heights to be above the top of the PBL, particularly for PC_PLR (Fig. 8b). This reflects the higher vertical development seen in Fig. 6b, likely caused by the static MODIS fire size used in PC_PLR.

The low PBL heights compared to MISR's higher plume tops are due partially to MISR's overpass time. Specifically, comparisons in the Northern Hemisphere must be done prior to 1030 LST. WRF-Chem's low PBL heights also may be related to the delayed heating caused by insufficient heat flux in the surface layer (Pagowski, 2004). Although current results indicate that most emissions escape the simulated PBL, further testing at other times and locations is needed to verify the current results. However, based solely on the Russian and Canadian plumes in our study, limiting injections to the PBL does not appear to be an adequate parameterization. A second simple alternative to a 1-d plume model has been to inject emissions in the 3-5 km layer. However, current results show that the alternative agrees poorly with observed heights (Fig. 8). Very few of the matched plumes are injected above 3 km. The triangle in Fig. 8 above the diagonal but below the yellow shading represents the most common injection layer, above the PBL but below the 3 km level. Additional evaluations in other areas and other meteorological settings are needed to confirm these results.

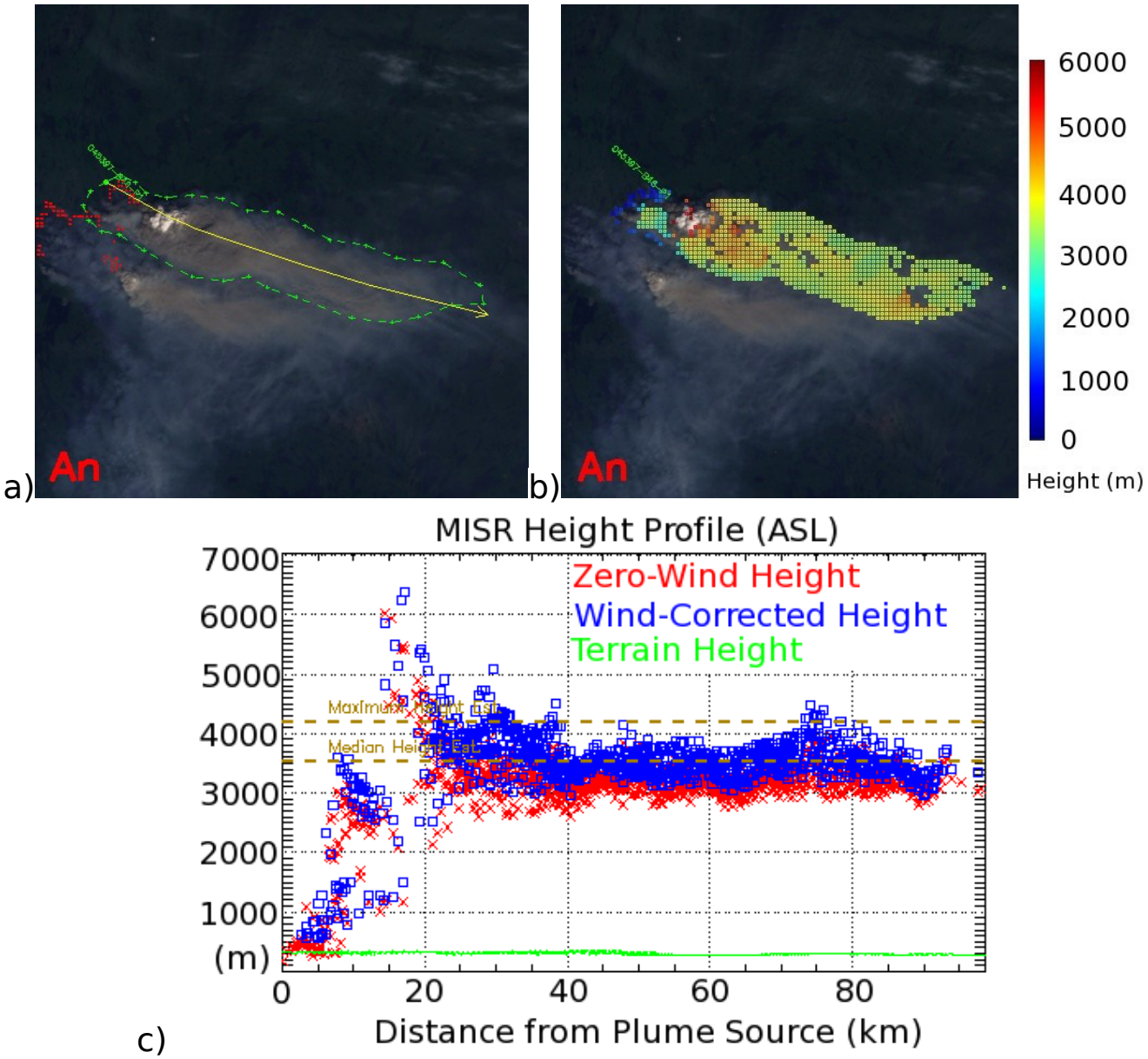

Fig. 5. Example of plume digitization produced by the MINX software package for a Canadian plume on 30 June 2008. Panel a) shows a smoke cloud (outlined in green) with associated MODIS fire pixels (red dots). Panel b) depicts the same plume with a stereo-height overlay. The label "An" in panels (a) and (b) indicates that these are nadir images. Panel c) shows individual stereo-heights within the plume in relation to their distance from the source. Planar maximum and median plume heights are shown as dashed lines. MINX images courtesy the MISR Plume Height Climatology Project. (http://www-misr2.jpl.nasa.gov/EPA-Plumes/)

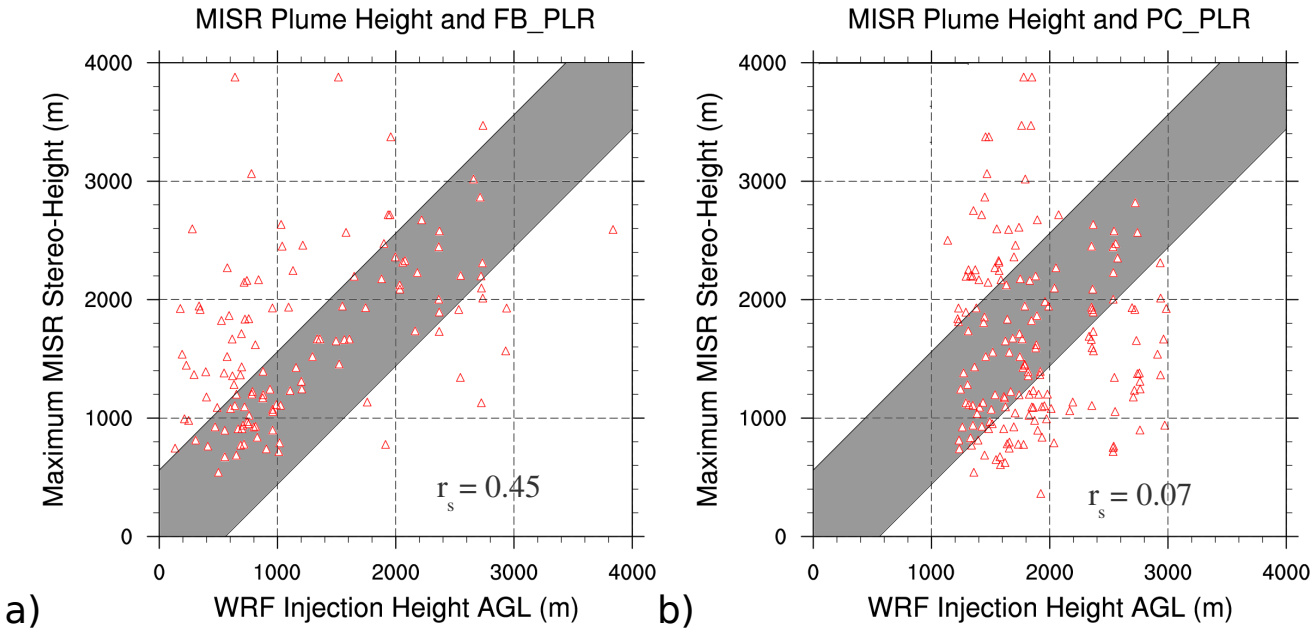

Fig. 6. a) Injection heights using FB_PLR plotted against MISR maximum stereo-heights for the entire ten day model run. b) Same as a), but based on PC_PLR. Shaded regions represent a hypothetical perfect correlation with MISR when assuming a stereo-height error of ± 560 m. Spearman correlation coefficients (r_s) are inset.

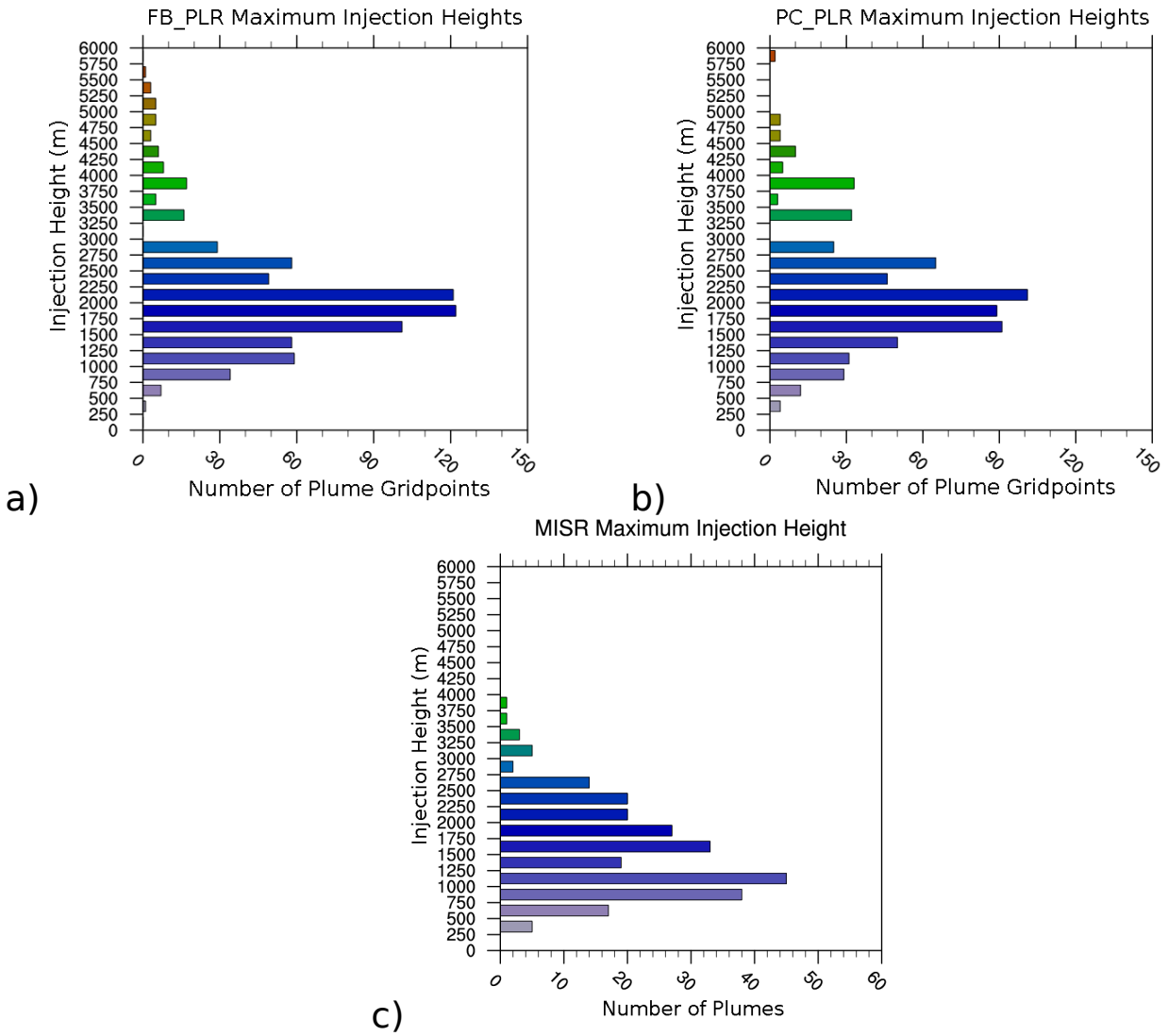

Fig. 7. Distribution of WRF-Chem maximum injection heights over Siberia and Canada during the entire ten day simulation period for a) FB_PLR and b) PC_PLR biomass burning emissions. c) MISR stereo-height distribution for the same period. Note the difference in scale between c) and a-b).

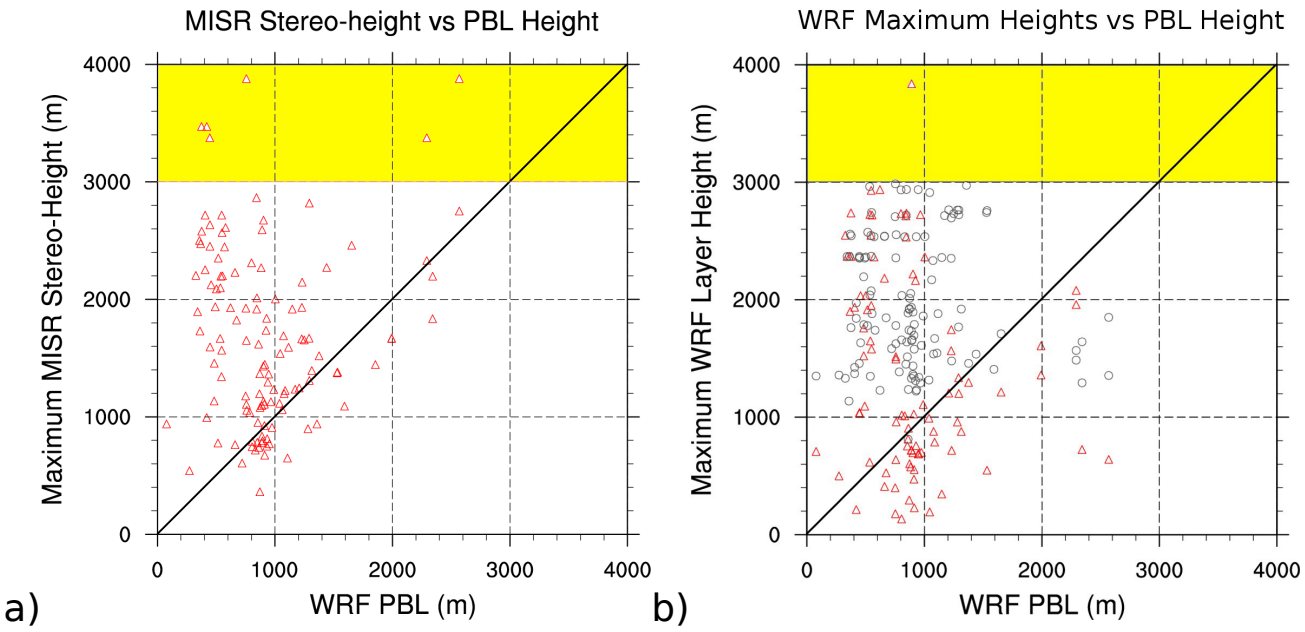

Fig. 8. a) MISR stereo-heights for ARCTAS plumes plotted against PBL heights from WRF-Chem. b) Maximum simulated injection heights for PC_PLR (blue circles) and FB_PLR (red triangles) plotted against simulated PBL heights. Points above the diagonal in a) represent MISR injections above the simulated PBL. The yellow shaded region represents the lower half of the injection layer for the 35K simulations.

3.3 LONG RANGE TRANSPORT

The previous section evaluated different injection height methodologies at the locations of the fires. We now describe how these varying heights influence long range plume transport.

3.3.1 Observed Long Range Transport

We first describe the evolution of the AIRS Level 3 total column CO product during the 10 day simulation period. CO patterns from WRF-Chem then will be examined against each other and to AIRS, which will serve as our standard for comparison. Although a potential low bias in the AIRS data over northern latitudes and the sensor's weak sensitivity in the boundary layer may prevent accurate measurement in some regions (J. Warner, personal comm.; Warner et al., 2007), general patterns still can be deduced. Fig. 9a shows a large CO plume over Russia and China with extensions over the Pacific Ocean on 28 June. This Russian plume was observed during the week prior to our integration period (not shown) as a combination of smaller wildfire outbreaks over the region together with another plume from the south in China. Since these plumes formed prior to our period of interest, and were not part of the initial conditions, we allowed WRF-Chem four days to advect these older plumes out of the study area before beginning quantitative evaluations on 2 July.

Beginning on 2 July (Fig. 9c), the dominant transport pathway from Russia extends over the Sea of Okhotsk northward over the Kamchatka Peninsula. The saddle point is still intact at this time (not shown), restricting the bulk of plume flow eastward over the northern Pacific Ocean. Small CO concentrations can be seen north of the Chukotski Peninsula. By 6 July (Fig. 9e), the saddle point has dissipated, permitting flow around the quasi-stationary polar low to advect larger concentrations of CO northbound toward the Bering Straight and the Arctic. This panel clearly displays the two transport routes mentioned earlier. On 8 July (Fig. 9f), the AIRS-derived CO diffuses across the Pacific; however, partial cloud cover prevents retrievals in the Arctic north of Canada and Greenland.

Although the Canadian CO plumes are much smaller than those from Russia (Fig. 10a,c), they do exhibit a simpler single path over the Atlantic Ocean. Their CO signal can be seen early during the study period spreading from central Canada to south of Hudson and James Bays (Fig. 9b). The plume is produced by fires located along the axis of Canada's glacial lakes, primarily in Saskatchewan. CO first is transported east-south-eastward across the central provinces. Then, flow around the low pressure systems keeps the plumes south of Hudson Bay and Greenland before they are transported over the North Atlantic (Fig. 9e). The major influence of California fires and the Russian plume can be seen on 6-8 July (Fig. 9e,f).

3.3.2 Simulated Russian Transport

The remainder of this chapter compares plumes from three model configurations with each other and with the observed satellite data. This is done both qualitatively (with CALIOP and AIRS) and quantitatively (with AIRS). In addition to injections into the PBL (FB_PBL) and from the 1-d plume model (FB_PLR), we also consider emissions that initially are limited to model levels between 3 and 5 km AGL (FB_35K). Plumes from Russia are examined first. The three configurations (FB_PLR, FB_PBL, FB_35K) initially exhibit similar horizontal plume shapes (Fig. 11a,c,e) with flow over the Sea of Okhotsk and subsequent branching southward and northward. These branches appear similar to those observed in the AIRS CO data (Fig. 9c) except that the simulated plumes are located slightly farther northwest, not over the southern tip of the Kamchatka Peninsula (Fig. 11a,c,e). Through 5 July (not shown), FB_PBL's plume over the Chukotski Peninsula maintains a southeastward pattern that results in the formation of a branch into the Arctic near the Date Line by 6 July (Fig. 11f). Conversely, plumes from FB_PLR and FB_35K are stretched northward by 6 July (Fig. 11b,d) west of FB_PLR where the saddle point has begun dissipating (Fig. 3b,d). AIRS also places a region of high CO concentration over the Chukotski Peninsula, but it extends over the Bering Straight (Fig. 9e), agreeing better with FB_PLR and FB_35K. Although low level transport over fire locations in FB_PBL produces a large southbound plume over China (Fig. 11f), we did not include it in our quantitative analysis that follows due to the difficulty in distinguishing it from local anthropogenic

sources. Much of it was filtered out of the AIRS data due to cloud coverage. The differences in plume locations seen in Fig. 11 occur because the FB_PLR and FB_35K plumes are transported northward above the PBL while FB_PBL is diverted on a more eastbound course by lower level flow.

Vertical cross sections of simulated aerosol plumes along the CALIPSO track (Fig. 12) allow comparisons of transport altitudes. The 6 July CALIPSO overpass at 0100 UTC crosses the dateline near 30N, heading northwest over the Chukotski Peninsula (Fig. 12a). This path passes over the northbound plume arch in Fig. 11b,d and the FB_PBL (Fig. 11f) plume over the North Pacific Ocean. The cross sections from FB_PLR and FB_35K (Fig. 12b,d) show similarities, with the Arctic-bound plume core lofted to between 3 and 7 km. FB_PLR exhibits an especially large concentration at ~7 km (Fig. 12b). The FB_PBL plume (Fig. 12f) is being advected northeast at a much lower altitude (~2 km) than the other two plumes. The major CALIOP feature (right half of Fig. 12e) agrees best with the FB_PLR and FB_35K plume locations (Fig. 12b,d). The attenuated backscatter shows the feature extending from ~10 km down to 4 km where the signal becomes completely attenuated. The CALIOP feature algorithm (Vaughan et al., 2004) determined this lower layer to be primarily cloud rather than aerosols. All three simulations place a small pocket of aerosols at the southern (left) edge of the cross section. However, this area is masked by clouds that are associated with a frontal system. Crawford et al. (2003) found cloud formations such as this to contain enhanced levels of emissions, creating problems for remotely sensed data. Thus, the ~3 km layer of cloud water above the WRF plume prevents successful aerosol feature identification. The presence of the FB_PLR and FB_35K plumes over the Chukotski peninsula is further corroborated in the AIRS CO data (Fig. 9e).

To quantitatively evaluate CO structures from the three WRF-Chem configurations against those from AIRS, we chose total column CO data on 2 July and 6 July (Fig. 11). MODE's object-based evaluation (see section 2.3.2) produces several statistical scores. We will consider the critical success index (CSI) whose values range from 0 (no skill) to 1 (perfect forecast). It must be noted that MODE scores are limited by the quality of the AIRS data. We did insure that areas masked in the AIRS data by clouds also were masked in the model fields when compared. This can either hurt or help the score, depending on the accuracy of the region removed; for example, if WRF-Chem overestimates a large plume, but it is in a region without AIRS data, the error is removed and the score is spuriously increased. The discussions that follow will note when large regions of the simulated plumes have been masked by missing AIRS data. Fig. 13 shows CSI scores for all simulated plumes on the two days selected for comparison. The modeled Asian plumes (RU_0702 and RU_0706) exhibit the largest scores of all plumes during the period, with FB_PLR (0.52) and FB_35K (0.49) scoring better than FB_PBL (0.42) on 2 July, four days into the simulation. These early plume scores improve on 6 July (RU_0706) when the CSI scores for FB_PLR (0.71) and FB_35K

(0.67) significantly increase. The smaller scores on 2 July likely are influenced by the presence of emissions in the AIRS data that originated before our modeling period began. FB_PBL's relatively low score (0.41) on 6 July probably results from under representing the emissions over the northern Chukotski Peninsula. The spreading of the simulated plumes into China (Fig. 11) could not be evaluated since the region is largely masked by clouds in the AIRS product (Fig. 9e).

3.3.3 Simulated Arctic Transport

We next examine the three versions of the Russian plume's northbound extension as they are transported into the Arctic during two major episodes (see Fig. 14). On 3 July (Fig. 14a,c,e), all three model configurations show an intrusion between 160 and 180 E. On the following day, weak AIRS CO enhancements reach the North Pole (Fig. 9d). The modeled plumes also reach the pole on 4 July (not shown) before slowing transporting toward Svalbard on 6 July. The model plumes differ primarily in size, with FB_35K being noticeably larger. However, the AIRS data near the pole during 3-5 July is low quality and can not used for further comparison. The three simulated plumes enter the Arctic at similar altitudes ~6 km (left side of Fig. 15b,d,f) after being lofted over the Chukotski Peninsula. The emissions from FB_PBL and FB_35K are transported into the mid- and upper-troposphere earlier than those of FB_PLR, producing an anticyclonic hook shaped deformation across the date line (Fig. 14c,e). Previous studies have shown warm conveyor belts associated with middle latitude cyclones to be an important mechanism for transporting Asian plumes into the Arctic's upper troposphere; they also have been found to be important to the vertical redistribution of emissions (e.g., Ding et al., 2009; Kiley and Fuelberg, 2006). The current transport to the Arctic also is primarily lofted by a warm conveyor belt.

The second Arctic transport event occurs during the final two days of the model period. It is part of the larger Russian plume seen in Fig. 9e. On 8 July, the northern arched portion of the Russian plume (Fig. 14b,d,f) extends to the western hemispheric portion of the Arctic Ocean, and southward along the Bering Straight. All three simulations continue to show distinctive characteristics this late into the ten day integration period. The 3 July intrusion has been transported across Svalbard and over the North Atlantic. FB_PLR and FB_35K continue to exhibit the most similarity (Fig. 14b,d), with their simulated plumes advecting along coastal Alaska and approaching Canada's Queen Elizabeth Islands. The vertical distribution of these two simulated plumes generally follows the isentropic surfaces (Fig. 16b,d), sloping slightly downward toward the pole. FB_PBL's second entrance into the Arctic is earlier than the other runs (Fig. 11f), resulting in weaker emission loading near North America and enhanced transport toward Europe (Fig. 14f).

This second Arctic event can be investigated further using CALIOP data. Unfortunately, several cloud features in the 2000 UTC 7 July polar overpass again inhibit aerosol retrievals. The VFM (Fig. 16e) shows only a small pocket of lower tropospheric aerosols in the two cloud features (denoted by arrows) that correspond to the FB_PLR and FB_35K plumes in Fig. 16b,d. Although these two leftmost simulated plumes follow the isentropes down towards the pole, the first (labeled 1 in Fig. 16e) CALIOP cloud feature does not slope or extend as far south (to the left in the plot). However, the isentropic slope of the second observed feature (labeled 2 in Fig. 16e) is closely matched by the two simulations. FB_PBL's single aerosol core approximately matches the first CALIOP feature (Fig. 16f) but lacks any similarity with the location of the AIRS CO plume (Fig. 9f). The clouds observed by CALIOP likely are the cause of the missing AIRS CO feature on 8 July. Nonetheless, a weak AIRS CO enhancement near the Queen Elizabeth islands is evident (Fig. 9f), supporting both FB_PLR and FB_35K (Fig. 14b,d). Despite being lofted to similar altitudes as the other two configurations (Fig. 16b,d,f), the winds associated with FB_PBL's early entrance into the Arctic steer the plume away from North America resulting in a completely different transport path (Fig. 14f).

The large differences between the simulated plume structures (Fig. 14) manifests itself in the CSI scores (Fig. 13). FB_PBL and FB_35K are most similar on 3 July, and the MODE-derived scores (AR_0703) provide confirmation (0.21 and 0.18, respectively). However, both are much less than FB_PLR (0.46). The smaller scores reflect the "hook" seen in Fig. 14c,e, a result of arriving in the Arctic prior to FB_PLR, and not being observed in the AIRS data. For the 8 July comparisons (AR_0708), a large portion of the Arctic AIRS data along the Date Line has been filtered out due to cloud contamination (Fig. 9f), limiting the evaluation to structures near the Queen Elizabeth Islands. This region of contamination causes MODE to remove the same region from the modeled data. This almost completely masks the FB_PBL plume, producing a much lower score (0.12) than either FB_PLR (0.27) or FB_35K (0.38). Despite having similar boundaries, the much weaker CO concentrations near North America prevent portions of the FB_PLR plume from being convolved into a MODE object for evaluation purposes. FB_35K's greater emission concentrations at the primary transport level produce stronger agreement with the AIRS data. Both sets of Arctic CSI scores are smaller than those of RU_0702 and RU_0706, likely a result of AIRS' data limitations over the high latitudes.

3.3.4 Simulated North American Transport

Long range emission transport across the North Pacific to North America and from Canada over the North Atlantic is examined next. The southern branch of the previously described Russian plume (Fig. 3) is steered by westerly winds associated with the southern portion of the Aleutian low. Its simulated CO

emissions reach the eastern Pacific by 3 July. Since all three WRF-Chem configurations produce similar transport patterns, we only will present FB_35K (Fig. 17). Transport occurs along 30 N (Fig. 17a) at ~5.3 km and then spread diffluently off the west coast of North America (Fig. 17c). A small portion of the plume branches off and continues northward to the Aleutians. The majority of the plume is transported anticyclonically southward before merging with California wildfire emissions over the U.S. Rocky Mountains (not shown). The 'scoop' shape of the modeled plume west of Canada on 5 July (Fig. 17a) occurs as a mid-latitude cyclone passes between the Aleutian Low and British Columbia. This shape also is observed in the AIRS CO retrievals (Fig. 9c). However, the timing of scoop development is earlier in the AIRS data than the simulations. By 6 July, the western portion of the plume near the Date Line has stretched south of 40 N (Fig. 17c) causing the three simulated plumes to align into a more linear southwest to northeast orientation. The CALIOP retrievals (Fig. 18b) reveal two features: a combination of cloud and aerosols over the Eastern Pacific Ocean between 2 km and 5 km (labeled 1) and a large cloud dominated feature near Alaska (labeled 2). The southern East Pacific feature is well represented in the simulations (Fig. 18d, FB_35K shown). It is located between approximately 2 km and 5 km with a downward slope on the southern (left) side of the plume core. The larger feature near Alaska is a combination of Asian and North American emissions from California and Oregon.

The major plume from the Canadian wildfires begins on 1 July. The emissions from fires between Great Slave Lake and Reindeer Lake first move southward due to northerly winds and then eastward across Lake Winnipeg (Fig. 17b). This region contains little AIRS CO data because of clouds, but an enhancement is evident over James Bay (Fig. 9c). The weaker simulated concentrations that connect the primary plume core to James Bay (Fig. 17b) are emissions from the Alaskan fires on 28-29 June. By 6 July, the mid-latitude cyclone responsible for the southward transport has moved east, producing more westerly flow (Fig. 3h). Variations in injection heights among the simulations have little effect on the modeled Canadian plumes. The developing plumes are rapidly transported over the warm sector of the passing cyclone where they are lofted to similar transport altitudes. The plumes from all three simulations pass over central Canada at ~3.0 km and ~3.8 km over Quebec before being transported over the North Atlantic.

Once over the Atlantic on 6-8 July, a portion of the Canadian fire plume is transported northward toward Greenland by the closed low over Hudson Bay (Fig. 17d). This creates a split region of CO just south of Greenland that is visible in the AIRS imagery (Fig. 9f). This bifurcation is similar to the branching seen in the Russian plume over the Sea of Okhotsk (left panels of Fig. 11). Unlike the Russian plume, the northern branch does not fully develop, sending most emissions zonally across the Atlantic Ocean (Fig. 17d). The southern portion of this offshore plume is centered at ~4.0 km, with the core of the northern most point near Greenland being lofted to ~6.8 km (left side, Fig. 19d), producing a downward slope toward the

south. The segment rising toward Greenland corresponds to two cloud features in the CALIOP data (labeled 1 and 2, Fig. 19b). The VFM (Fig. 19b) shows aerosol enhancements (label 1) near the surface and into the upper troposphere between the clouds. The corresponding model plumes (Fig. 19d) exhibit aerosols near this observed core, but they also contain additional emissions that slope southward (to the right) toward the surface. The CALIOP data do not support this extended mid-level southern branch. Above and south (right) of that feature, Fig. 19d shows a second weaker aerosol feature between 6 km and 11 km. The CALIOP VFM shows pockets of aerosols around the cloud base (labeled 2, Fig. 19b). The model plume cores and observed cloud feature (Fig. 19b,d) both exhibit a slight downward slope to the north (left), with the model cores ~2 km lower than observed. The small Arctic plume in Fig. 11c reappears between Iceland and the United Kingdom (Fig.16d) after crossing the North Pole. It is unique to the FB_35K simulation.

MODE-derived CSI scores for the Eastern Pacific and Canadian plumes vary little between the three model configurations (Fig. 13), indicating the importance of the early lofting by the warm conveyor belt. Over Canada, we compare early emission outflow on 2 July (CA_0702) and 7 July (CA_0707) when significant simulated transport over the Atlantic Ocean occurs. Scores for CA_0702 generally are small (FB_PLR, 0.27; FB_35K, 0.31; FB_PBL, 0.31; Fig. 13), a result of comparing numerous objects that are fractured and masked by cloud cover west of James Bay (Fig. 9c). However on CA_0707, two large plume structures can be evaluated, one leaving Quebec and the other farther over the North Atlantic. The models show these to be components of a single plume that has been spuriously separated by data quality and a break in satellite coverage south of Newfoundland where the overpasses converge. The CSI scores on this day are larger than before because the plumes are more cohesive. Nonetheless, there is no clearly superior model configuration (FB_PLR, 0.39; FB_35K, 0.40; FB_PBL, 0.42). In general, all of the Canadian scores suffer from a combination of missing data or poor data assimilation. Emissions from Russia released before the integration period are visible off the western North American coast in Fig. 9a,b. However, without ingesting them into WRF-Chem, it quickly becomes difficult to make a fair comparison of emissions known to be solely from North American fires. Clouds also are a consistent hindrance to satellite retrievals as observed in Fig. 10.

CSI scores for the Eastern Pacific plumes (EP_0705 and EP_0706; Fig. 13) are opposite those of the Canadian scenario, with the later plume (EP_0706) scoring worse than the earlier. The first comparison is of the southward dip off the southern Alaskan coast on 5 July that is present in each of the simulations (Fig. 17a). It also is present in the AIRS data (not shown), but almost 12 h prior to when simulated. Nonetheless, it still compares favorably with the tail end of the observed scoop (Fig. 17a), resulting in moderate CSI scores (FB_PLR, 0.42; FB_35K, 0.41; FB_PBL, 0.39; Fig. 13). The comparisons for 6 July (EP_0706) produce much smaller CSI scores (FB_PLR, 0.29; FB_35K, 0.27; FB_PBL, 0.26). While both the forecast

and observed objects now have a more linear structure along the southern edge of the Aleutian low (Figs. 16c, 9e), each forecast plume is rotated clockwise, making landfall farther south near Vancouver Island. This comparison is eight days into the simulation and is closest to the lateral boundary of any plume. Both factors potentially cause faulty transport meteorology. The simulations also produce a southbound plume feature (Fig. 17c) that is not present in the AIRS CO data. The absence of this feature may be due to its descent toward the surface where AIRS has less sensitivity.

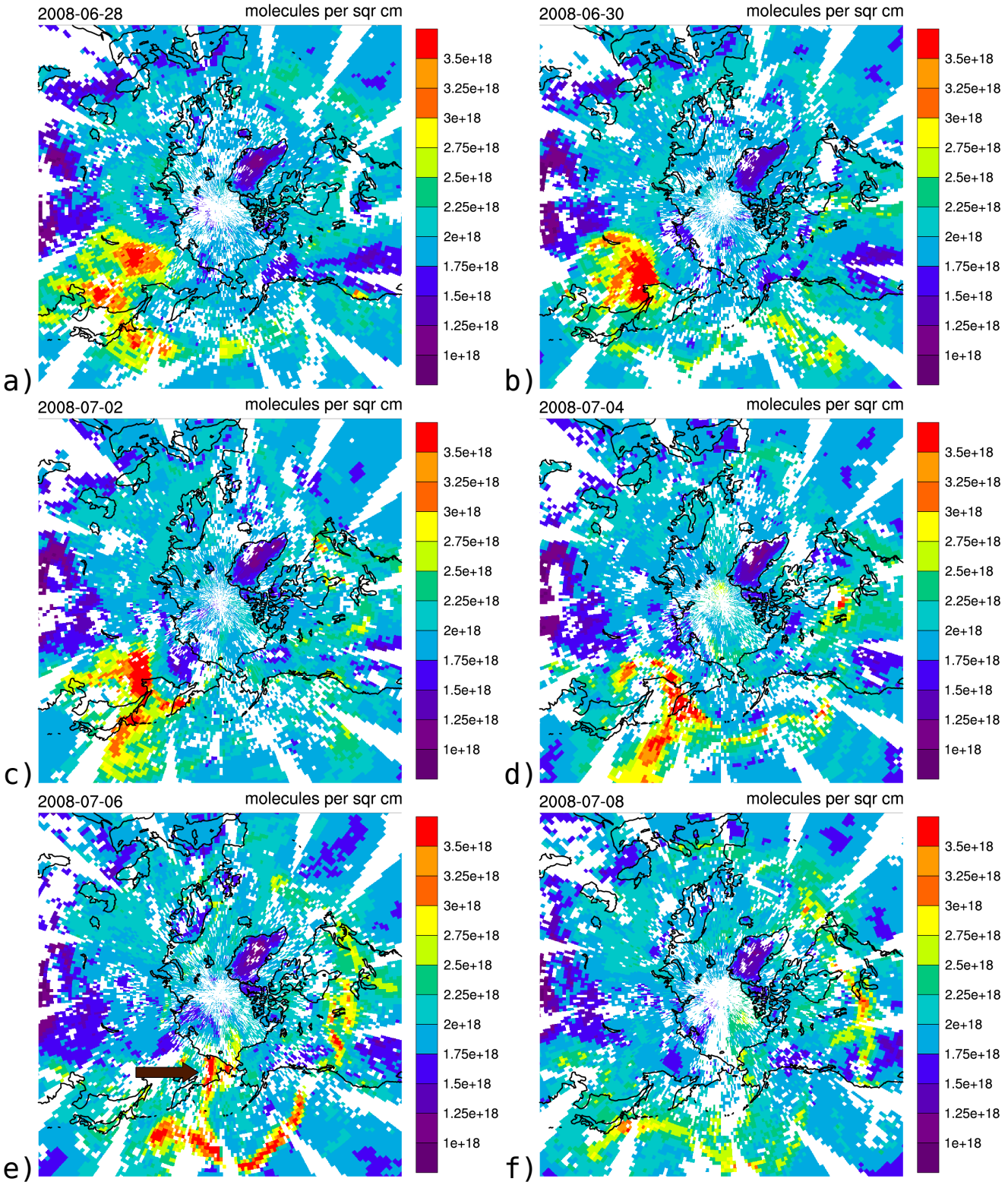

Fig. 9. AIRS 1 × 1 deg Level 3 Total Column CO (molecules cm^{-2}) between 28 June - 8 July 2008. The arrow in panel e) is the second plume discussed in the Arctic long range transport section.

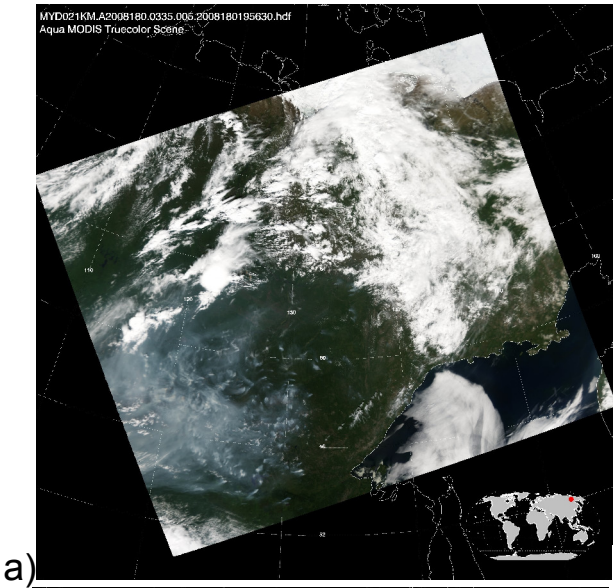

a)

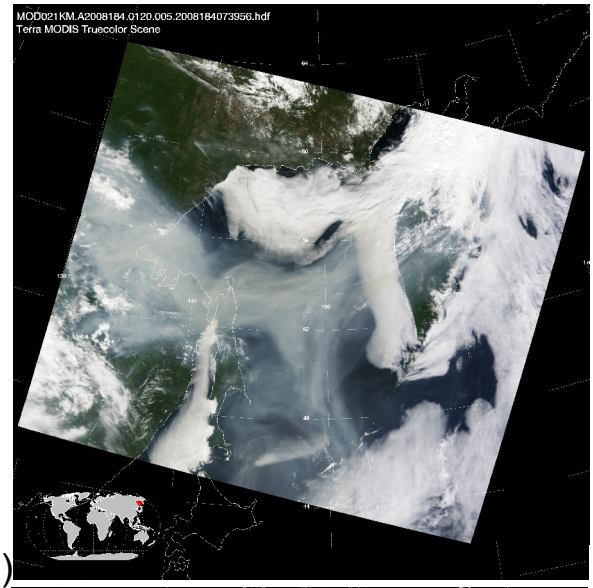

b)

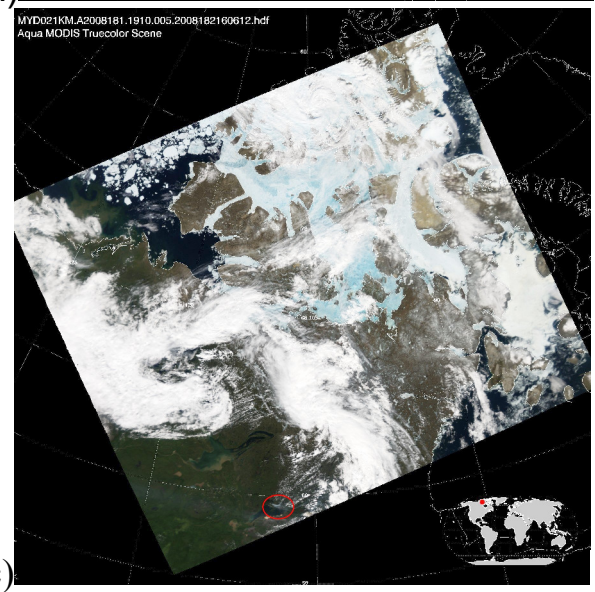

c)

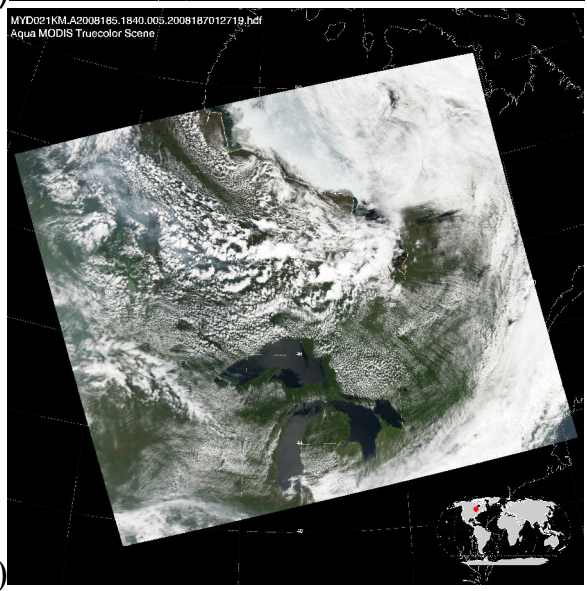

d)

Fig. 10. a) Russian fires on 28 June 2008 and b) subsequent offshore plume transport on 2 July 2008. c) Canadian fires on 29 June 2008 are less widespread and are obscured by clouds, with the Lake Athabasca fire being the most visible (circled in red). d) Clouds and smoke being advected between the Great Lakes and Hudson Bay on 3 July 2008. MODIS images a), c) and d) are from the Aqua satellite, while b) is from Terra. Images courtesy the NASA Goddard Space Flight Center (http://modis-atmos.gsfc.nasa.gov/)

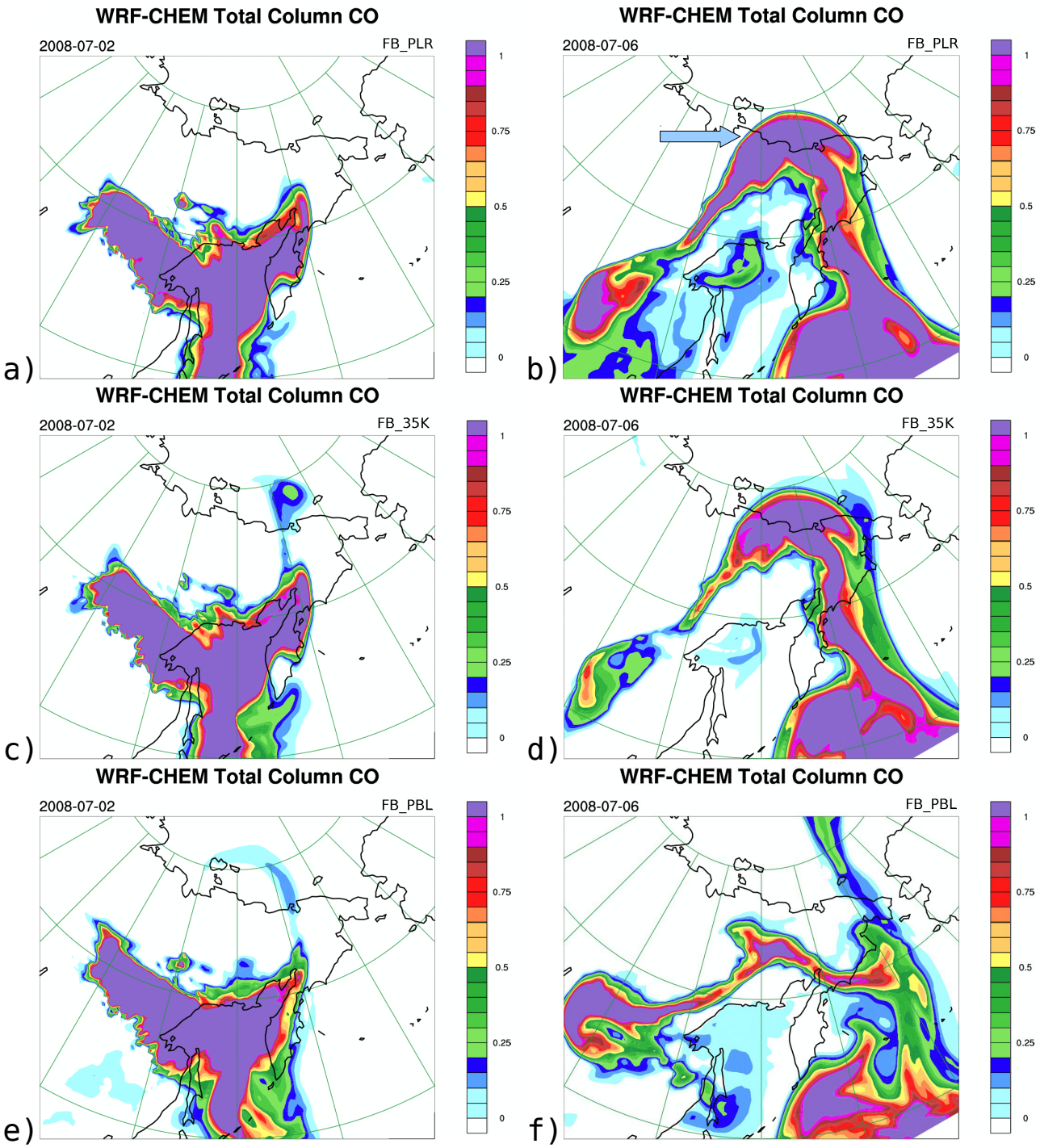

Fig. 11. Normalized WRF-Chem Total Column CO for the Russian plume over Asia and the western Pacific Ocean for a,b) FB_PLR, c,d) FB_35K, and e,f) FB_PBL for a,c,d) 2 July and b,d,e) 5 July 2008. The arrow in panel b) denotes one of the plumes discussed in the Arctic transport section.

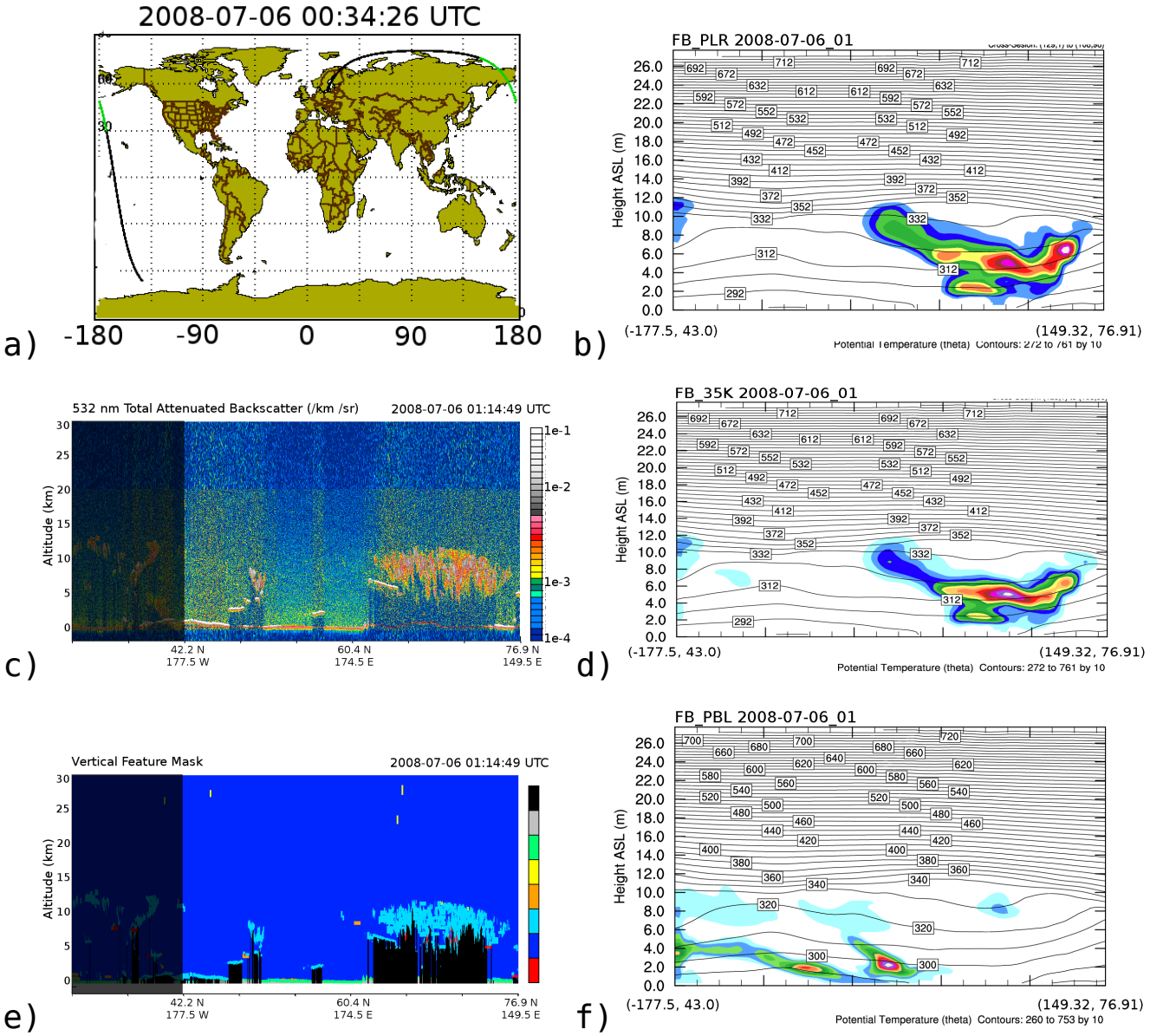

Fig. 12. a) Map of CALIPSO path at 0100 UTC 6 July 2008 with the analyzed segment over Russia in green, c) CALIOP 532 nm attenuated backscatter, and e) the CALIOP vertical feature mask (VFM). Normalized WRF aerosol plumes for b) FB_PLR, d) FB_35K, and f) FB_PBL along the CALIPSO track. The left side of each cross section is the south eastern starting point, while the right side is the north western ending point. In panel e), orange and cyan represent aerosols and clouds, respectively. CALIPSO imagery courtesy the NASA Langley Research Center.

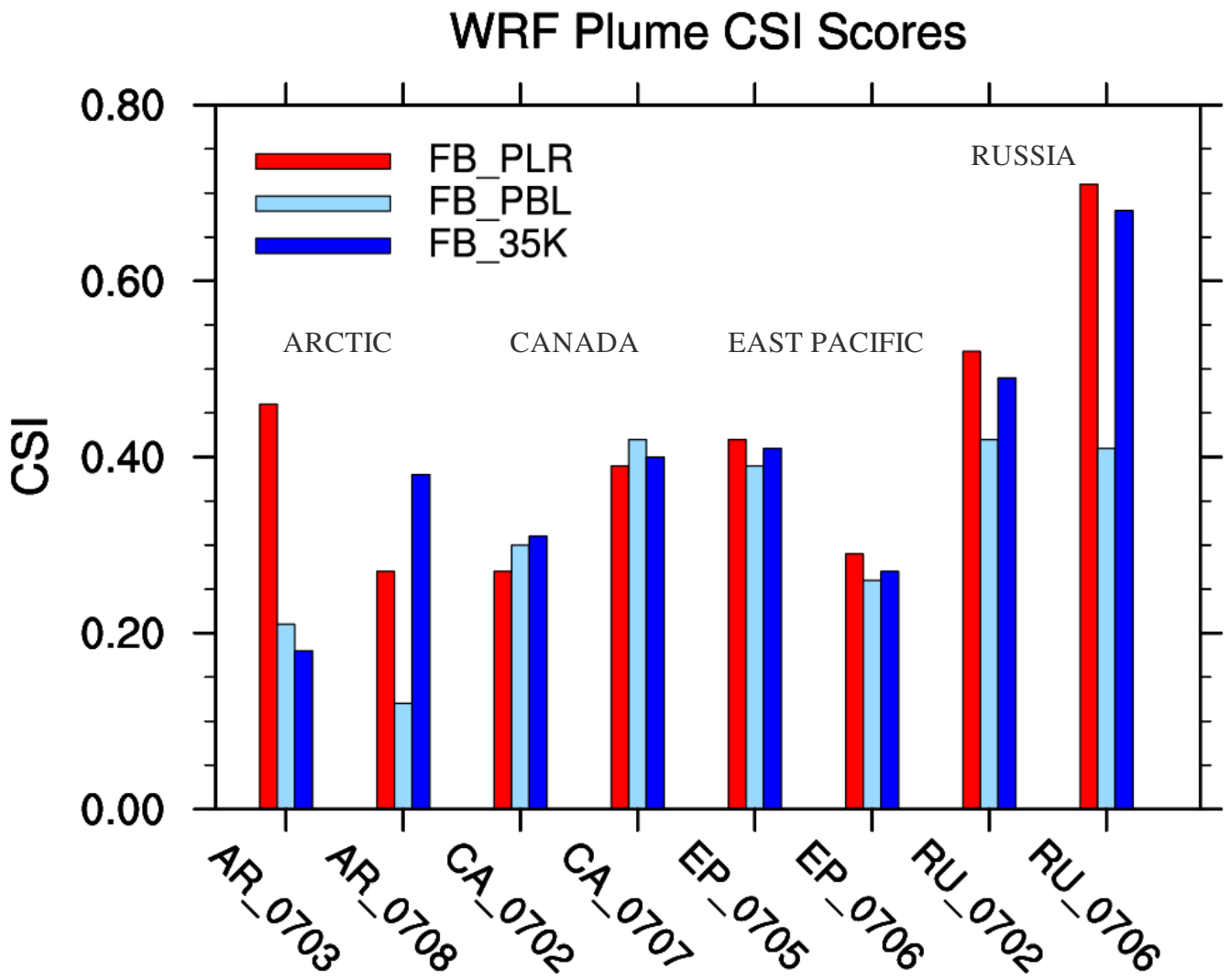

Fig. 13. Critical Success Index scores for the three WRF-Chem configurations of total column CO plumes compared to AIRS total column data. Each triplet represents the scores for a particular plume described in the text. Plumes include Arctic intrusions (AR), the Canadian plume (CA), long range transport over the Eastern Pacific (EP), and the near-source Russian plume over the Sea of Okhotsk and the Western Pacific (RU). Numbers represent the month and day in 2008 (mmdd).

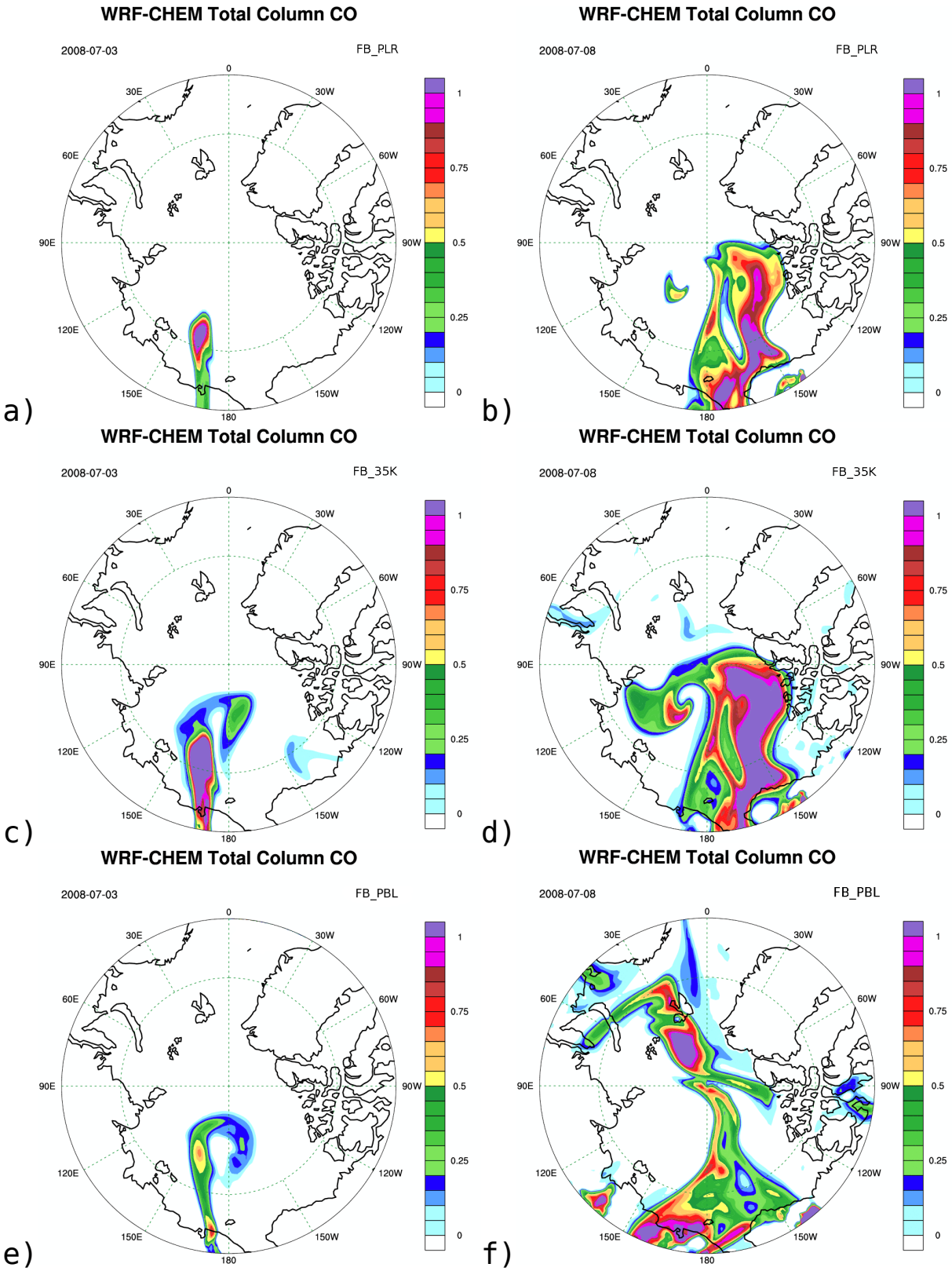

Fig. 14. Normalized WRF-Chem Total Column CO for the northern branch of the Russian plume over the Arctic Ocean for a,b) FB_PLR, c,d) FB_35K, and e,f) FB_PBL on a,c,d) 4 July and b,d,e) 8 July 2008.

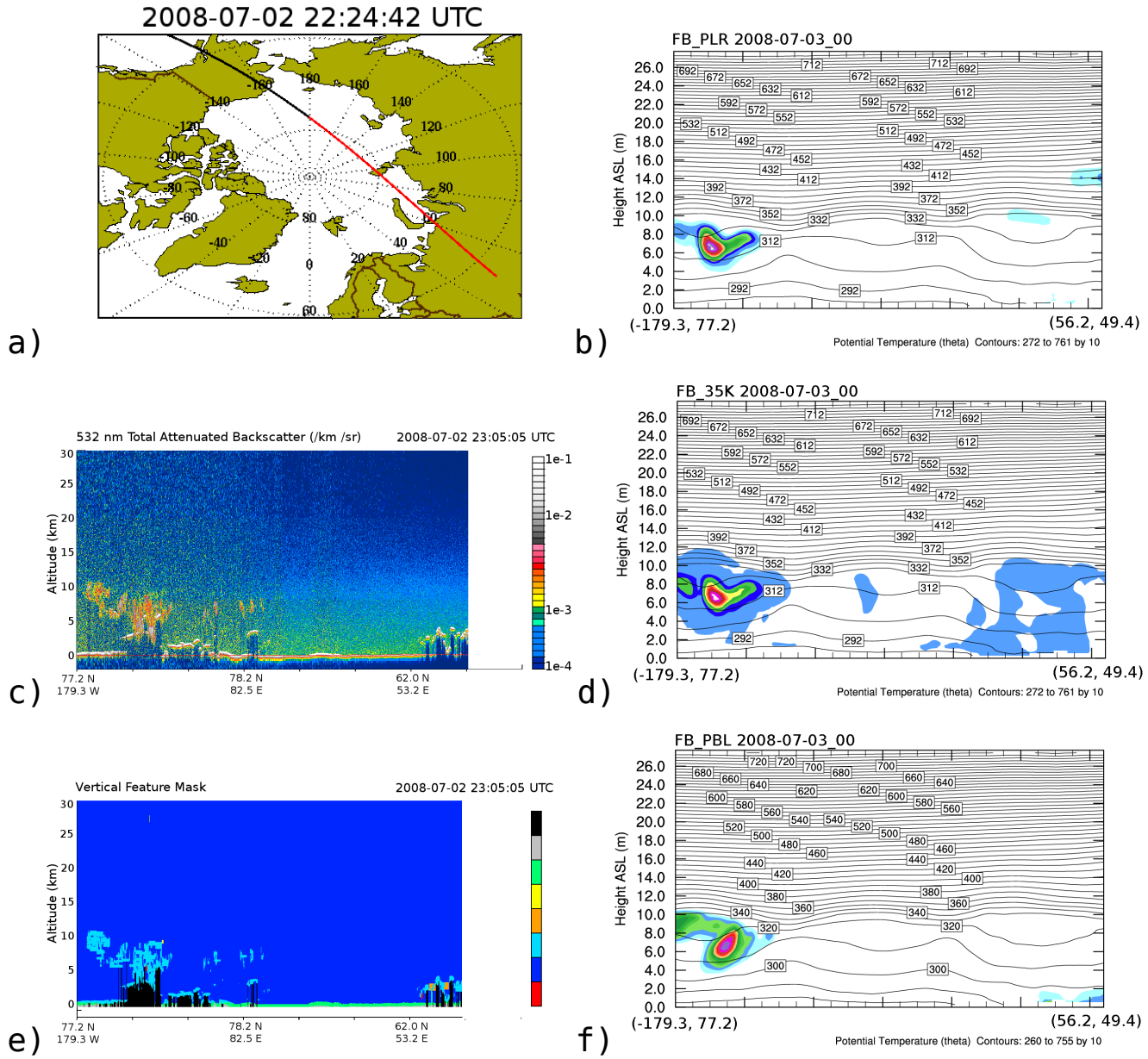

Fig. 15. a) Map of CALIPSO path at 2300 UTC 3 July 2008 with analyzed segment near the North Pole in red, c) CALIOP 532 nm attenuated backscatter, and e) the CALIOP vertical feature mask (VFM). Normalized WRF aerosol plumes for b) FB_PLR, d) FB_35K, and f) FB_PBL along the CALIPSO track. In panel e), orange and cyan represent aerosols and clouds, respectively

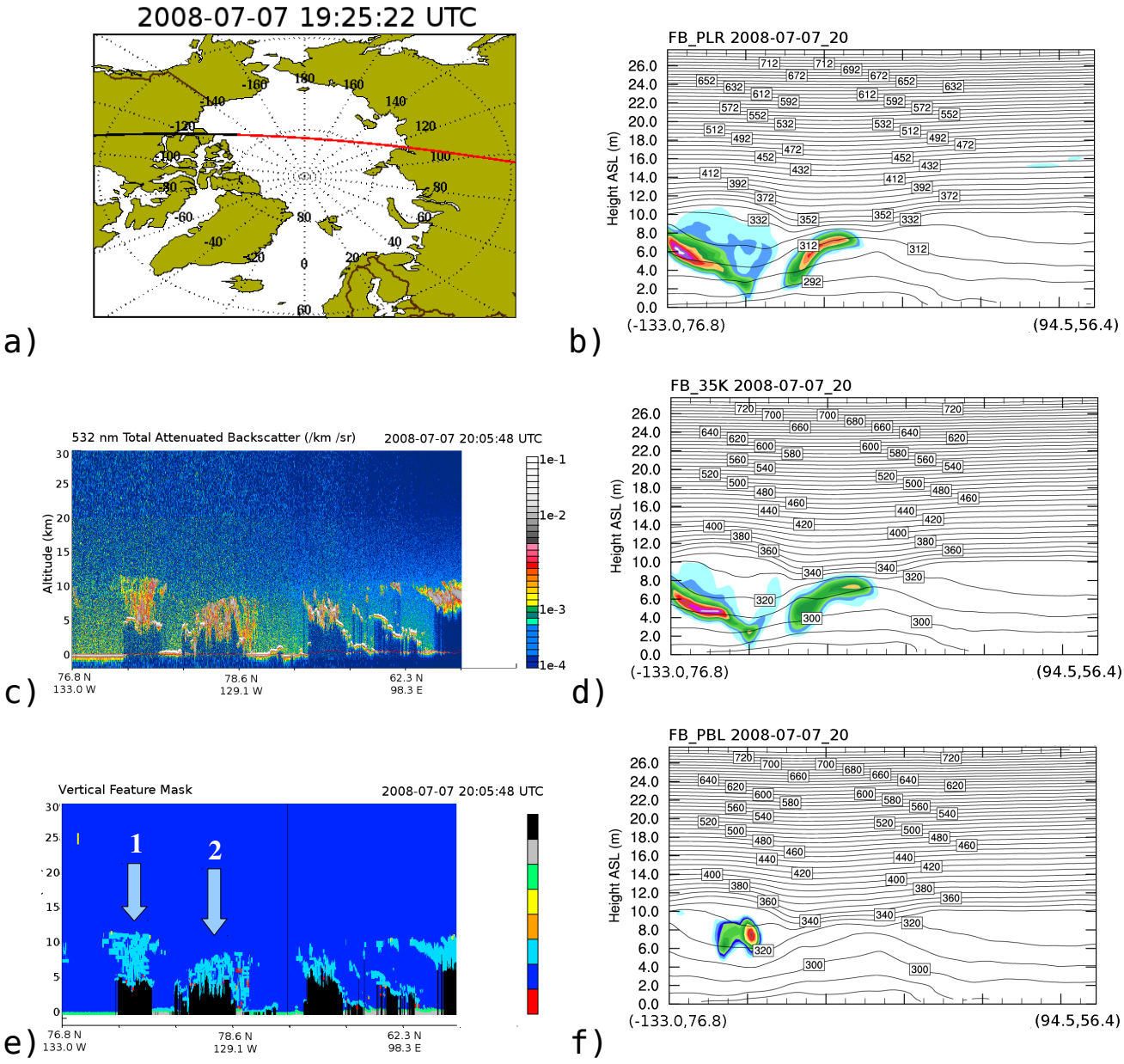

Fig. 16. Map of CALIPSO path at 2000 UTC 7 July 2008 with analyzed segment near the North Pole in red, c) CALIOP 532 nm attenuated backscatter, and e) the CALIOP vertical feature mask (VFM). Normalized WRF aerosol plumes for b) FB_PLR, d) FB_35K, and f) FB_PBL along the CALIPSO track. Arrows in panel e) represent features compared in the text. In panel e), orange and cyan represent aerosols and clouds, respectively

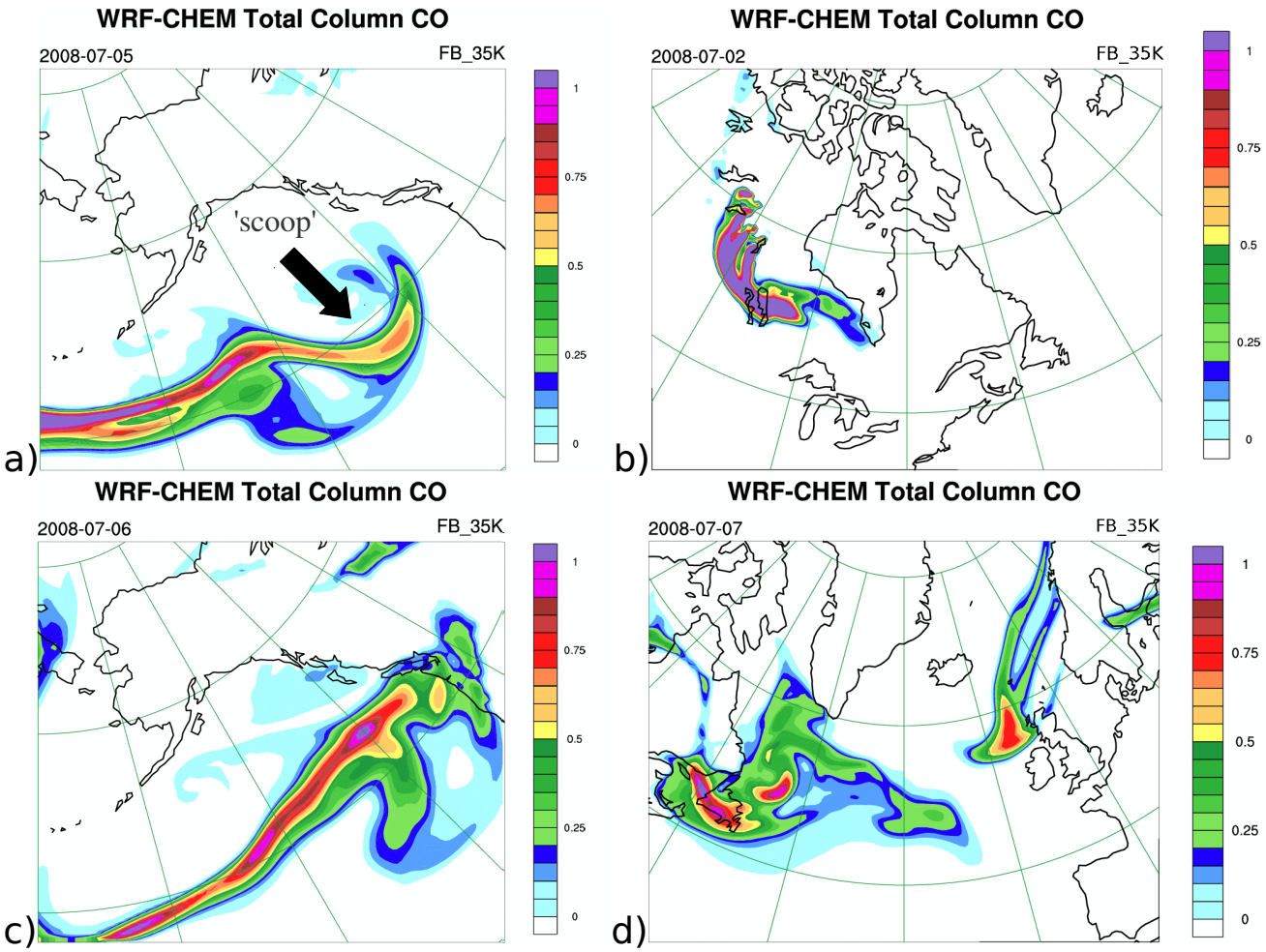

Fig. 17. Normalized WRF Total Column CO (FB_35K) for the North American plume over Canada on b) 2 July and over the North Atlantic on d) 7 July. Normalized WRF Total Column CO for the southern branch of the Russian plume over the eastern Pacific Ocean on a) 5 July and c) 6 July.

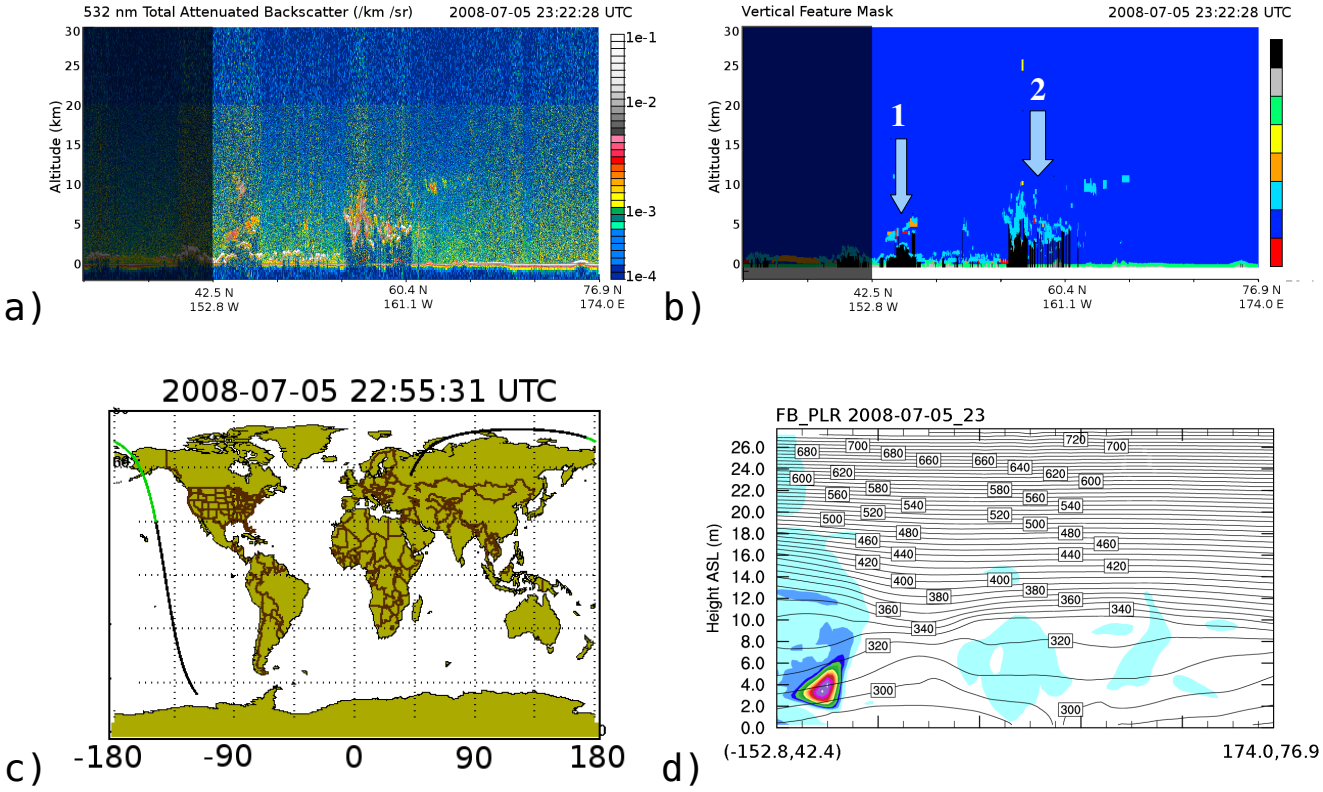

Fig. 18. a) CALIOP 532 nm attenuated backscatter, b) CALIOP vertical feature mask (VFM), c) map of CALIPSO path at 2300 UTC 5 July 2008 with analyzed segment near Alaska in green, and d) the normalized WRF aerosol plume for FB_PLR along the CALIPSO track.

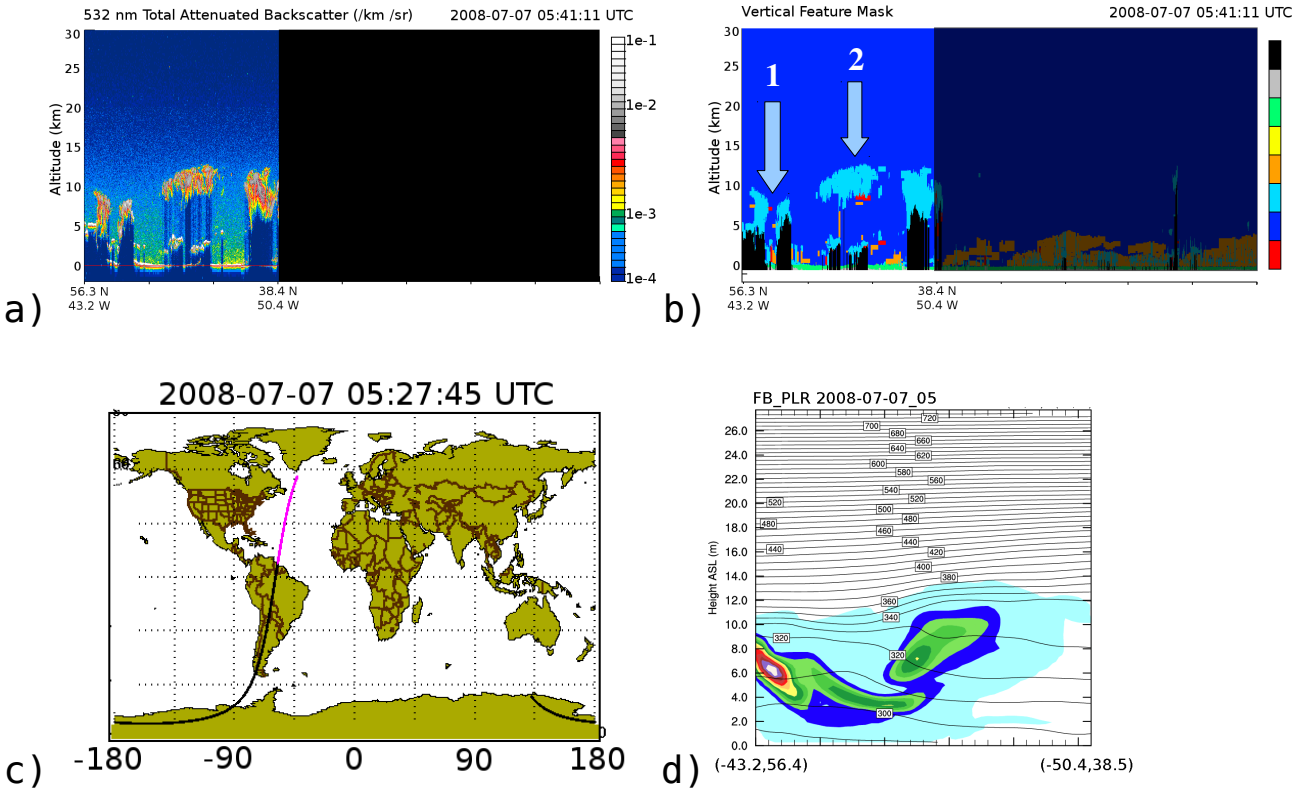

Fig. 19. a) CALIOP 532 nm attenuated backscatter, b) CALIOP vertical feature mask (VFM), c) map of CALIPSO path at 0500 UTC 7 July 2008 with analyzed segment over the Atlantic Ocean in violet, and d) the normalized WRF aerosol plume for FB_PLR along the CALIPSO track. This is a descending overpass; north is to the left in a), b), and d). Arrows in b) indicate features discussed in the text. In panel b), orange and cyan represent aerosols and clouds, respectively

CHAPTER FOUR

SUMMARY AND CONCLUSIONS

The sensitivity of the Arctic environment to anthropogenic and biomass burning emissions from lower latitudes necessitates constant monitoring of its atmosphere. In addition to knowing what is occurring now, we must accurately forecast potential threats. Large scale episodic events such as boreal wildfires represent direct air quality threats to population areas as well as secondary effects caused by modifying the Arctic environment. To accurately simulate these events, it is important not only to represent the transport meteorology but also to inject wildfire emissions at appropriate altitudes.

This study has examined WRF-Chem's ability to diagnose the injection layers of biomass burning emissions by comparing simulations against satellite-derived plume heights from the MISR sensor aboard the Terra satellite. Ten day simulations were performed during the ARCTAS period of Summer 2008. The model was run using two separate preprocessing methods for wildfires, prep_chem_sources and FLAMBE. Prep_chem_sources produced a narrow distribution of injection heights due to how the plume rise model parameterizes entrainment. Plume height is reduced by entrainment, which is inversely proportional to the burn area that is input to the model. The majority of the fires studied were identified by MODIS, to which prep_chem_sources applied a single burn area value, regardless of the time of day. This constant value limited the range of injection heights.

FLAMBE produced a wider range of injection layers that more closely agreed with the MISR-derived heights. Although FLAMBE begins with a single burn area per detection, the areas then are modified to be proportional to the diurnal cycle of burning intensity, with size increasing during the afternoon and decreasing at night. The inclusion of smaller burn areas during the morning produced lower injection heights that were more consistent with those observed during MISR's morning overpass.

We also used the MISR stereo-heights to evaluate two column filling emission methods that have been widely used—emissions confined to the planetary boundary lower, and emissions released between 3 km and 5 km AGL. The majority of the MISR stereo-heights were found above the simulated planetary boundary layer but below the 3-5 km layer. This indicated that emissions limited to these layers were not ideal for the geographic and meteorological settings of the study. The majority of injection heights simulated by the WRF-Chem plume rise model also were between the PBL top and 3 km AGL indicating that during the study period, the plume rise model presented the most realistic approximation of the top of injection layers.

Simulated long range plume transport was evaluated both qualitatively and quantitatively against data from the AIRS and CALIOP satellite sensors. Quantitative scores were produced using an object-based

method in the MODE software package. We focused on three methods of emissions (plume rise, FB_PLR; planetary boundary layer, FB_PBL; 3-5 km AGL, FB_35K) using only the FLAMBE dataset. Results for these emission configurations were compared for plumes over four regions: an eastern Russian plume over the Sea of Okhotsk, the northern branch of the Russian plume transported into the Arctic, the southern branch transported across the Pacific Ocean, and a Canadian plume over eastern Canada and the Atlantic Ocean.

Results showed that differences between injection methods were most important when source emissions were not immediately influenced by synoptic scale lofting mechanisms such as warm conveyor belts. When large scale lofting mechanisms were absent, different transport patterns were able to develop because of the different injection heights. This different transport was most evident in the northern branch of the Russian plume and its subsequent transport into the Arctic. The higher emission layers from FB_PLR and FB_35K were transported into the Arctic over the Chukotski Peninsula, while the lower altitude FB_PBL emissions were lofted much later and followed a different path. Satellite data supported the higher altitude emission schemes over northeastern Russia and into the Arctic. And, MODE-derived scores confirmed that the plume rise configuration produced the best agreement with the satellite observations. An exception was the final day over the Arctic when clouds limited the comparison of observed and simulated plumes.

Our long range transport evaluations were limited by two considerations. First, satellite data quality was compromised in heavily clouded regions such as central Canada and the Arctic, particularly for the final comparison (AR_0708). This was problematic since emissions often are transported within clouds. Large regions of the simulated Canadian and Arctic plumes could not be qualitatively or quantitatively compared because of cloud contamination. The presence of emissions released prior to the study period also produced observed enhancements over Canada and Russia that were unrepresented in the simulations. This problem could be reduced with the assimilation of satellite-derived CO data into WRF-Chem. Improvements in satellite data quality would enhance the WRF-Chem simulations during with input and later during verification.

To summarize, use of the one-dimensional plume rise model within WRF-Chem produced injection heights and plumes that agreed best with observed data during our study period. The greatest differences between injection methods occurred in cases of delayed exposure to large scale lofting influences such as warm conveyor belts. This was the case with the Arctic bound segment of the Russian plume. Differences were smaller when synoptic influences were closer to the plume source, such as in Canada and the southern branch of the Russian plume. Systematic weaknesses also were present in our quantitative comparisons due to clouds obscuring satellite retrieval areas.

The current results are based on a small study period within the Arctic summer. Additional studies should be performed to determine whether they are applicable to other regions and seasons.

REFERENCES

Ackermann, I.J., Hass, H., Memmesheimer, M., Ebel, A., Binkowski, F.S., Shankar, U.: Modal aerosol dynamics model for Europe: development and first applications. Atmos. Environ., 32, 2981–2999, 1998.

Andreae, M. O., and Merlet, P.: Emission of trace gases and aerosols from biomass burning, Global Biogeochem. Cy., 15, 955–966, 2001.

Andreae, M. O., Rosenfeld, D., Artaxo, P., Costa, A. A., Frank, G. P., Longo, K. M., and Silva-Dias, M. A. F.: Smoking rain clouds over the Amazon, Science, 303, 1337–1342. 2004.

Hassol, S. J.: Impacts of a Warming Arctic: Arctic Climate Impact Assessment, Cambridge Univ. Press, New York, 2004

Badr, O., and Probert, S. D.: Carbon monoxide concentration in the Earth's atmosphere, Appl. Energ., 49, 99–143, 1994.

Barrie, L.A., Arctic air pollution: An overview of current knowledge, Atmos. Environ., 20, 643-663, 1986.

Berry, E. X.: Modification of the warm rain process, Preprints, 1st Natl. Conf. on Weather Modification, Am. Meteorol. Soc., Albany, NY, 81–88, 1968.

Byram, G. M.: Combustion of Forest Fuels, in: Forest Fire: Control and Use, Davis, K. P. (ed.), McGraw-Hill, New York, 61-89, 1959.

Chang, J.S., Binkowski, F.S., Seaman, N.L., McHenry, J.N., Samson, P.J., Stockwell, W.R., Walcek, C.J., Madronich, S., Middleton, P.B., Pleim, J.E., Lansford, H.H.: The regional acid deposition model and engineering model. State-of-Science/Technology, Report 4, National Acid Precipitation Assessment Program, Washington, DC, 1991.

Cofer, W. R., Winstead, E. L., Stocks, B. J., Overbay, L. W., Goldammer, J. G., Cahoon, D.: Emissions from boreal forest fires: Are the atmospheric impacts underestimated? In: Biomass Burning and Global Change, Levine, J. S. (ed.), MIT Press, Cambridge, MA, 834-839, 1996.

Colarco, P. R., Schoeberl, M. R., Doddridge, B. G., Marufu, L. T., Torres, O., and Welton, E. J.: Transport of smoke from Canadian forest fires to the surface near Washington, D. C.: Injection height, entrainment, and optical properties, J. Geophys. Res., 109 , D06203, doi:10.1029/2003JD004248, 2004.

Damoah, R., Spichtinger, N., Forster, C., James, P., Mattis, I., Wandinger, U., Beirle, S., Wagner, T., and Stohl, A.: Around the world in 17 days – hemispheric-scale transport of forest fire smoke from Russia in May 2003, Atmos. Chem. Phys., 4, 1311–1321, 2004,

Diner, D. J., Davies, R., DiGirolamo, L., Horvath, A., Moroney, C., Muller, J. P., Paradise, S. R., Wenkert, D., and Zong, J.: MISR level 2 cloud detection and classification algorithm theoretical basis, JPL D-11399, Rev. D, Jet Propulsion Laboratory, California Institute of Technology, 1999.

Ding, A., Wang, T., Xue, L. K., Gao, J., Stohl, A., Lei, H. C., Jin, D. Z., Ren, Y., Wang, X. Z., Wei, Z. L., Qi, Y. B., Liu, J., and Zhang, X. Q.: Transport of north China air pollution by midlatitude cyclones: Case

study of aircraft measurements in summer 2007, J. Geophys. Res., 114, D08304, doi:10.1029/2008JD011023, 2009.

Fisher, J.A., Jacob, D. J., Purdy, M. T., Kopacz, M., Le Sager, P., Carouge, C., Holmes, C. D., Yantosca, R. M., Batchelor, R. L., Strong, K., Diskin, G. S., Fuelberg, H. E., Holloway, J. S., Hyer, E. H., McMillan, W. W., Warner, J., Streets, D. G., Zhang, Q., Wang, Y., Wu, S., Source attribution and interannual variability of Arctic pollution in spring constrained by aircraft (ARCTAS, ARCPAC) and satellite (AIRS) observations of carbon monoxide, Atmos. Chem. Phys., 10, 977-996, 2010.

Freitas, S. R., Longo, K. M., Chatfield, R., Latham, D., Silva Dias, M. A. F., Andreae, M. O., Prins, E., Santos, J. C., Gielow, R., and Carvalho Jr., J. A.: Including the sub-grid scale plume rise of vegetation fires in low resolution atmospheric transport models, Atmos. Chem. Phys., 7, 3385–3398, 2007.

Freitas, S. R., Longo, K. M., Trentmann, J., and Latham, D.: Technical Note: Sensitivity of 1-D smoke plume rise models to the inclusion of environmental wind drag. Atmos. Chem. Phys. Discuss., 9, 14713–14733, 2009.

Fromm, M., Shettle, E. P., Fricke, K. H. Ritter, C., Trickl, T., Giehl, H., Gerding, M., Barnes, J. E., O'Neill, M., Massie, S. T. Blum, U., McDermid, I. S., Leblanc, T., and Deshler, T.: Stratospheric impact of the Chisholm pyrocumulonimbus eruption: 2. Vertical profile perspective, J. Geophys. Res-Atmos., 113, D08203, doi: 10.1029/2007JD009147, 2008.

Garrett, Tim: Pollutant Haze is Heating up the Arctic. http://earthobservatory.nasa.gov/Newsroom/view.php?id=30036,10 May 2006.

Generoso, S., Bey, I., Attie, J.-L., Breon, F.-M.: A satellite- and model-based assessment of the 2003 Russian fires: Impact on th Arctic Region, J. Geophys. Res-Atmos., 112, D15302, doi:10.1029/2006JD008344, 2007.

Giglio, L., Descloitres, J., Justice, C. O., and Kaufman, Y. L.: An enhanced contextual fire detection algorithm for MODIS, Remote Sens. Environ., 87, 273–282, doi:10.1016/S0034-4257(03)00184-6, 2003.

Global Climate and Weather Modeling Branch: The GFS Atmospheric Model. NOAA/NWS/NCEP Office Note 442, 14 pp., 2003.

Grell, G. A., Peckham, S. E., Schmitz, R., McKeen, S. A., Frost, G., Skamarock, W. C., and Eder, B.: Fully coupled “online” chemistry within the WRF model, Atmos. Environ., 39, 6957-6975, doi:10.1016/j.atmosenv.2005.04.027, 2005.

Hegg, D. A., Warren, S. G., Grenfell, T. C., Doherty, S. J., Larson, T. V., and Clarke, A. D.: Source attribution of black carbon in arctic snow, Environ. Sci. Technol., 43, 4016-4021, doi:10.1021/es803623f, 2009.

Justice, C. O., Giglio, L., Korontzi, S., Owens, J., Morisette, J. T., Roy, D., Descloitres, J., Alleaume, S., Petitcolin, F., and Kaufman, Y.: The MODIS fire products, Remote Sens. Environ., 83, 244-262, 2002.

Kahn, R. A., Li, W.-H., Moroney, C., Diner, D. J., Martonchik, J. V., and Fishbein, E.: Aerosol source plume physical characteristics from space-based multiangle imaging, J. Geophys. Res., 112, D11205, doi:10.1029/2006JD007647, 2007.

Kahn, R. A., Chen, Y., Nelson, D. L., Leung, F. Y., Li, Q. B., Diner, D. J., and Logan, J. A.: Wildfire smoke

injection heights: two perspectives from space, Geophys. Res. Lett., 35, L04809, doi: 10.1029/2007GL032165, 2008.

Kasischke, E. S., and Bruhwiler, L. P.: Emissions of carbon dioxide, carbon monoxide, and methane from boreal forest fires in 1998, J. Geophys. Res., 107, 8146, doi:10.1029/2001JD000461, 2002.

Kasischke, E. S., Hyer, E. J., Novelli, P. C., Bruhwiler, L. P., French, N. H. F., Sukhinin, A. I., Hewson, J. H., and Stocks, B. J.: Influences of boreal fire emissions on Northern Hemisphere atmospheric carbon and carbon monoxide, Global Biogeochem. Cy., 19, GB1012, doi:10.1029/2004GB002300, 2005.

Kessler, E.: On the distribution and continuity of water substance in atmospheric circulations, Meteor. Monographs, 10, Am. Meteorol. Soc. Boston, MA, 1969.

Kiley, C. M., and Fuelberg, H. E.: An examination of summertime cyclone transport processes during intercontinental chemical transport experiment (INTEX-A), J. Geophys. Res., 111, D24S06, doi:10.1029/2006JD007115, 2006.

Klonecki, A., Hess, P., Emmons, L., Smith, L., Orlando, J., and Blake, D.: Seasonal changes in the transport of pollutants into the Arctic troposphere-model study, J. Geophys. Res., 108, 8367, doi:10.1029/2002JD002199, 2003.

Koch, D., and Hansen, J.: Distant origins of Arctic black carbon: A Goddard Institute for Space Studies ModelE experiment, J. Geophys. Res., 110, 4204, doi:10.1029/2004JD005296, 2005.

Labonne, M., Breon, F.-M., and Chevallier, F.: Injection height of biomass burning aerosols as seen from a spaceborne lidar, Geophys. Res. Lett., 34, L11806, doi:10.1029/2007GL029311, 2007.

Lamarque, J. F., Edwards, D. P., Emmons, L. K., Gille, J. C., Wilhelmi, O., Gerbig, C., Prevedel, D., Deeter, M. N., Warner, J., Zeskin, D. C., Khattatov, B., Francis, G. L., Yudin, V., Ho, S., Mao, D., Chen, J., and Drummond, J. R.: Identification of CO plumes from MOPPITT data: Application to th August 2000 Idaho-Montana forest fires, Geophys. Res. Lett., 30, 1688, doi:10.1029/2003GL017503, 2003.

Latham, D.: PLUMP: A one-dimensional plume predictor and cloud model for fire and smoke managers, General Technical Report INT-GTR-314, Intermountain Research Station, USDA Forest Service, Nov, 1994.

Law, K. S. and Stohl, A.: Arctic Air Pollution: Origins and Impacts, Science, 315, 1537-1540, 2007.

Lavoue, D., Liousse, C., Cachier, H., Stocks, B. J., and Goldammer, J. G.: Modeling of carbonaceous particles emitted by boreal and temperate wildfires at northern latitudes, J. Geophys. Res., 105, 26,871-26,890, 2000.

Levine, J. S., (ed.): Global Biomass Burning: Atmospheric, Climatic, and Biospheric Implications, The MIT Press, 569 pp., 1991.

Liu, S.C., McKeen, S. A., Hsie, E. Y., Lin, X., Kelly, K. K., Bradshaw, J. D., Sandholm, S. T., Browell, E. V., Gregory, G. L., Sachse, G. W., Bandy, A. R., Thornton, D. C., Blake, D. R., Rowland, F. S., Newell, R., Heikes, B. G., Singh H., and Talbot, R. W.: Model study of tropospheric trace species distributions during PEM-West A, J. Geophys. Res., 101, 2073-2085, 1996.

Martin, M. V., Logan, J. A., Kahn, R. A., Leung, F. Y., Nelson, D. L., and Diner, D.: Smoke injection heights from fires in North America: analysis of 5 years of satellite observation, Atmos. Chem. Phys., 10, 1491-1510, 2009.

Mass, C.F., Ovens, D., Westrick, K., and Colle, B. A.: Does Increasing Horizontal Resolution Produce More Skillful Forecasts? The results of two years of real-time numerical weather prediction over the Pacific northwest, B. Am. Meteorol. Soc., 83, 407-430, 2002.

Matson, M., and Dozier, J.: Identification of subresolution high temperature sources using a thermal IR sensor, Photogramm. Eng. Rem. S., 47, 1311-1318, 1981.

McConnell, J. R., Edwards, R., Kok, G. L., Flanner, M. G., Zender, C. S., Saltzman, E. S., Banta, J. R., Pasteris, D. R., Carter, M. M., and Kahl, J. D. W.: 20th-century industrial black carbon emissions altered arctic climate forcing, Science, 317, 1381, doi:10.1126/science.1144856, 2007.

McMillan, W. W., Barnet, C., Strow, L., Chahine, M. T., McCourt, M. L., Warner, J. X., Novelli, P. C., Korontzi, S., Maddy, E. S., and Datta, S.: Daily global maps of carbon monoxide from NASA's Atmospheric Infrared Sounder, Geophys. Res. Lett., 32, L11801, doi:10.1029/2004GL021821, 2005.

Mellor, G.L., Yamada, T., 1982. Development of a turbulent closure-model for geophysical fluid problems, Rev. Geophys. Space. Ge., 20, 851–875, 1982.

Muller, J.-P. and Mandanayake, A. and Moroney, C. and Davies, R. and Diner, D.J. and Paradise, S.: MISR stereoscopic image matchers: techniques and results, IEEE T. Geosci. Remote., 40, 1547-1559, 2002.

Nelson, D. L., Chen, Y., Kahn, R. A., Diner, D. J., and Mazzoni, D.: Example applications of the MISR INteractive eXplorer (MINX) software tool to wildfire smoke plume analyses, Proc. SPIE, 7089, 708909.1–708909.11, 2008.

Ogura, Y. and Takahashi, T.: Numerical simulation of the life cycle of a thunderstorm cell, Mon. Weather Rev., 99, 895–911, 1971.

Peffers, L.: Evaluation of carbon monoxide dispersion in complex terrain using a lagrangian particle dispersion model driven by WRF output, M. S., Florida State University, Tallahassee, FL., 2009.

Pagowski, M.: Some comments on PBL parameterizations in WRF, The Joint WRF/MM5 Users' Workshop, Boulder, CO., 2004.

Quinn, P. K., Shaw, G., Andrews, E., Dutton, E. G., Ruoho-Airola, T., and Gong, S. L.: Arctic haze: current trends and knowledge gaps, Tellus B, 59, 99-114, doi:10.1111/j.1600-0889.2006.00238.x, 2007.

Quinn, P. K., Bates, T. S., Baum, E., Doubleday, N., Fiore, A. M., Flanner, M., Fridlind, A., Garrett, T. J., Koch, D., and Menon, S.: Short-lived pollutants in the Arctic: their climate impact and possible mitigation strategies, Atmos. Chem. Phys., 8, 1723-1735, 2008.

Reid, J., Hyer, E. J., Prins, E. M., Westphal, D. L., Zhang, J., Wang, J., Christopher, S. A., Curtis, C. A., Schmidt, C. A., Eleuterio, D. P., Richardson, K. A., and Hoffman, J. P.: Global Monitoring and Forecasting of Biomass-Burning Smoke: Description of and Lessons From the Fire Locating and Modeling of Burning Emissions (FLAMBE) Program, IEEE J. Sel. Top. Appl., 2, 2009.

Sachse, G. W., Hill, G. F., Wade, L. O., and Perry, M. G.: Fastresponse, high-precision carbon monoxide sensor using a tunable diode laser absorption technique, J. Geophys. Res., 92, 2071–2081, 1987.

Schell, B., Ackermann, I.J., Hass, H., Binkowski, F.S., Ebel, A.: Modeling the formation of secondary organic aerosol within a comprehensive air quality model system, J. Geophys. Res., 106, 28275–28293, 2001.

Schultz, M. G., Heil, A., Hoelzemann, J. J., Spessa, A., Thonicke, K., Goldammer, J. G., Held, A. C., Pereira, J. M. C., van het Bolscher, M.: Global wildland fire emissions from 1960-2000, Global Biogeochem. Cy., 22, GB2002, 10.1029/2007GB003031, 2008.

Skamarock W. C., Klemp, J. B., Dudhia, J., Gill, D. O., Baker, D. M., Duda, M. G., Huang, X., Wang, W., and Powers, J. G.: A description of the Advanced Research WRF version 3. NCAR Tech. Note NCAR/TN-475+STR, 113 pp., 2005.

Sharma, S., Andrews, E., Barrie, L. A., Ogren, J. A., and Lavoué, D, J.: Variations and sources of the equivalent black carbon in the high Arctic revealed by long-term observations at Alert and Barrow: 1989-2003, J. Geophys. Res.-Atmos., 111, D14208, doi: 10.1029/2005JD006581, 2006.

Shaw, G. E.: The Arctic haze phenomenon, B. Am. Meteorol. Soc., 76, 2403-2413, 1995.

Shindell, D., Faluvegi, G., Lacis, A., Hansen, J., Ruedy, R., and Aquilar, E.: Role of tropospheric ozone increases in 20th-century climate change, J. Geophys. Res.-Atmos., 111, D08302, doi: 10.1029/2005JD006348, 2006.

Solberg, S., Dye, C., Schmidbauer, N., Herzog, A., and Gehrig, R.: Carbonyls and non-methane hydrocarbons at rural European sites from the Mediterranean to the Arctic, J. Atmos. Chem., 25, 33-66, 1996.

Stockwell, W.R., Middleton, P., Chang, J.S., Tang, X.: The second-generation regional acid deposition model chemical mechanism for regional air quality modeling, J. Geophys. Res.-Atmos., 95, 16343–16367, 1990.

Stohl A., Hittenberger, M., and Wotawa, G.: Validation of the Lagrangian particle dispersion model FLEXPART against large scale tracer experiments. Atmos. Environ. 32, 4245-4264, 1998.

Stohl, A., Wotawa, G., Seibert, P., and Kromp-Kolb, H.: Interpolation Errors in Wind Fields as a Function of Spatial and Temporal Resolution and Their Impact on Different Types of Kinematic Trajectories. J. Appl. Meteorol., 34, 2149–2165, 1995.

Stohl, A., Forster, C., Frank, A., Seibert, P., and Wotawa, G.: Technical Note : The Lagrangian particle dispersion model FLEXPART version 6.2., Atmos. Chem. Phys., 5, 2461-2474, 2005.

Stohl, A.: Characteristics of atmospheric transport into the Arctic troposphere, J. Geophys. Res.-Atmos., 111, D11306, 10.1029/2005JD006888, 2006.

Stohl, A., Forster, C., Huntrieser, H., Mannstein, H., McMillan, W. W., Petzold, A., Schlager, H., and Weinzie, B.: Aircraft measurements over Europe of an air pollution plume from Southeast Asia – aerosol and chemical characterization, Atmos. Chem. Phys., 7, 913-937, 2007.

Susskind, J., Barnet, C. D., and Blaisdell, J. M.: Retrieval of atmospheric and surface parameters from AIRS/AMSU/HSB data in the presence of clouds, IEEE T. Geosci. Remote, 41, 390-409, 2003.

Trentmann, J., Luderer, G., Winterrath, T., Fromm, M., Servranckx, R., Textor, C., Herzog, M., Graf, H. F., and Andreae, M. O.: Modeling of biomass smoke injection into the lower stratosphere by large forest fire (Part I): Reference simulation, Atmos. Chem. Phys., 6, 5247-5260, 2006.

van der Werf, G.,, Rnderson, J. T., Collatz, G. J., and Giglio, L.: Carbon emissions from fires in tropical and subtropical ecosystems, Glob. Change Biol., 9, 547–562, 2003.

Vaughan, M., Young, S., Winker, D., Powell, K., Omar, A., Liu, Z., Hu, Y., and Hostetler, C.: Fully automated analysis of space-based lidar data: an overview of the CALIPSO retrieval algorithms and data products. Proc. SPIE, 5575, pp. 16-30, 2004.

Warner, J., Comer, M. M., Barnet, C. D., McMillan, W. W., Wolf, W., Maddy, E., and Sachse, G.: A comparison of satellite tropospheric carbon monoxide measurements from AIRS and MOPITT during INTEX-A, J. Geophys. Res., 112, D12S17, doi:10.1029/2006JD007925, 2007.

Warner, T.T., Peterson, R. A., and Treadon, R. E.: A Tutorial on Lateral Boundary Conditions as a Basic and Potentially Serious Limitation to Regional Numerical Weather Prediction. B. Am. Meteorol. Soc., 78, 2599-2617, 1997.

Winker, D. M., Hunt, W. H., and Hostetler, C. A.: Status and performance of the CALIOP Lidar, Proc. SPIE, 5575, 8–15, 2004.

Westphal, D. L., and O. B. Toon: Simulations of microphysical, radiative, and dynamical processes in a continental-scale forest fire smoke plume, J. Geophys. Res.-Atmos., 96, 22379–22422, 1991.

Wotawa, G., Novelli, P. C., Trainer, M., and Granier, C.: Inter-annual variability of summertime CO concentrations in the Northern Hemisphere explained by boreal forest fires in North America and Russia, Geophys. Res. Lett., 28, 4575– 4578, 2001.

Zhang, L., Jacob, D. J., Boersma, K. F., Jaffe, D. A., Olson, J. R., Bowman, K. W., Worden, J. R., Thompson, A. M., Avery, M. A., Cohen, R. C., Dibb, J. E., Flock, F. M., Fuelberg, H. E., McMillan, W. W., Singh, H. B., and Weinheimer, A. J.: Transpacific transport of ozone pollution and the effect of recent Asian emission increases on air quality in North America: an integrated analysis using satellite, aircraft, ozonesonde, and surface observations, Atmos. Chem. Phys., 8, 6117-6136, 2008 .

BIOGRAPHICAL SKETCH

Walter Sessions was born in Orlando, Florida on February 23, 1982. His family's involvement with aviation and agriculture led to an early interest in the weather. During middle and high school, he taught himself the fundamentals of computer programming and electronics, which occasionally shortened the lifespans of his family's computers. He also spent a great deal of time playing trombone in the school orchestral band as well as a local jazz ensemble. After graduating from Winter Park High School in May of 2000, he entered the meteorology program at Florida State University. After two years, Walter took a hiatus to work as an engineer for Varian Medical Systems near Boston, Massachusetts. His tasks ranged from designing hardware stress tests for cancer treatment devices to traveling around the world, troubleshooting in the field.

In 2005, Walter decided to return to FSU to complete his degree in meteorology. After receiving a Bachelor's of Science degree in Meteorology in 2007, he began working as a graduate research assistant under Professor Henry Fuelberg. During this time, Walter also acted as the Fuelberg Lab's systems administrator, maintaining a cluster of thirteen machines running Linux, Windows, and Solaris operating systems. The research opportunities with Prof. Fuelberg led to more travel as part of the NASA ARCTAS Field Mission. Walter enjoyed several science-minded flights on the NASA DC-8 in the high latitudes of Canada, experiencing both long range and near source sampling of fire emissions, occasionally *too* near source.

After the completion of his Master's of Science in Meteorology, Walter intends to continue modeling aerosol transport with the Naval Research Laboratory in Monterey, California.